Semiclassical predictions of cosmological wave packets from ridgelines

Chen Lan[*]
School of Physics, Nankai University, 94 Weijin Road, Tianjin 300071, China

Yi-Fan Wang[†]
Niologic GmbH, Max-Ernst-Str. 4, 50354 Hürth, Germany
and Institute for Theoretical Physics, University of Cologne, Zülpicher Str. 77a, 50937 Cologne, Germany

(Received 10 October 2021; accepted 22 November 2021; published 18 January 2022)

We introduce a concept of ridgelines to investigate the semiclassical predictions from wave packets with arbitrary widths in conventional quantum mechanics and the Wheeler–DeWitt quantum cosmology. Two primary approaches are applied to the exact calculation of the ridgelines, namely the contour and the stream approaches. Moreover, aspects of these are discussed and compared to other scenarios and approaches, i.e., the narrow WKB wave packets and the first-derivative test. As the main result, we show that the semiclassical predictions in toy models have more abundant solutions than the ones in the classical theory, and most interestingly they may deviate from classical solutions due to the quantum corrections.

DOI: 10.1103/PhysRevD.105.026002

I. INTRODUCTION

As the prevailing theory of gravitation, the general theory of relativity successfully describes classical gravitation, but has yet to be consistently quantized, despite the efforts of generations of physicists in over a hundred years.

One of the first attempts to quantize general relativity directly is the Wheeler–DeWitt approach, see e.g., [1,2]. It begins with the Hamiltonian formulation of this theory by Arnowitt, Deser and Misner, and applies the quantization scheme of Dirac, designed for constrained systems, including the Dirac spinors and the Maxwell theory, among others. This approach, also known as quantum geometrodynamics, is successful with the semiclassical methods of Wentzel–Kramers–Brillouin (WKB) [3] and Born–Oppenheimer [4], and has been applied to quantum models of universes and black holes.

Unfortunately, because of the constrained nature of general relativity (from another perspective, its diffeomorphism invariance), its quantized version à la Dirac lacks many properties that are crucial in conventional quantum theory. Particularly, a positive-definite scalar product of quantum states is difficult to define, rendering the nonexistence of a Hilbert space, and of the analysis of self-adjoint operators. As a consequence, one cannot use the usual way to make predictions as in conventional quantum mechanics. This includes, on the one hand, interpreting the inner product as a probability amplitude; on the other hand, analyzing self-adjoint operators and studying their spectra.

Quantum cosmology is an application of quantum geometrodynamics to the universe as a whole (see e.g., [[1], Ch. 8]), where the Wheeler–DeWitt equation plays the central role. The emergence of classical trajectories can be realized if the forms of *wave functions* are similar to the "coherent states," which strongly peak about a single classical trajectory [5]. However, such an analog of "coherent state" can only be achieved for simple examples.

In contrast, the emergence of classical trajectories from *wave packets* is relatively natural, where the wave packets of universe are constructed by the superposition of wave functions, and follow the classical trajectories in configuration space, when their widths become narrow [6–8]. This corresponds to the principle of constructive interference. Nevertheless, the correspondence between classical and quantum theories can only be implemented with the narrowness condition. In this work, we try to address these problems by porting conventional tools in physics and mathematics to this context, aiming to derive the classical predictions from wave packets with arbitrary widths.

The outline of topics in each section is as follows. In Sec. II, we summarize previous results of a two-dimensional minisuperspace model [9], which can be solved exactly and will be used as the basis to investigate the classical prediction from the corresponding wave packets in this paper. Next, under the WKB approximation, we show that a *narrow* Gaussian wave packet has "maxima" on the classical trajectory and can be compared to the one derived by the method of ridgelines discussed later, which works for wave packets with *arbitrary* widths. In Sec. III, we construct a framework of stationary wave packets that makes sense for both the minisuperspace

[*]lanchen@nankai.edu.cn
[†]yfwang@thp.uni-koeln.de

Wheeler–DeWitt equation and the stationary Schrödinger equation. The framework is then tested by the model of a two-dimensional hydrogen atom. In Sec. IV, the concept of ridgelines is introduced, and an intuitive approach, the first-derivative test, is applied to derive the ridgelines from wave packets. The deviation from classical theory emerges apparently near the turning point, which is interpreted as a quantum correction. In Secs. V and VI, we discuss two further approaches to find the ridgelines as classical predictions from wave packets with *arbitrary* widths, one is the contour approach, the other one is the stream approach. We provide exact mathematical descriptions of ridgelines, which were historically developed for Riemannian geometry with a Euclidean metric signature. Then we try to generalize these descriptions to the pseudo-Riemannian geometry with a Lorentzian metric signature, which is the usual case of minisuperspaces. After that, we apply both approaches in various examples, and discuss their advantages as well as deficits. Section VII includes a discussion of the relation between these two approaches. Finally, we give a summary and conclusion in Sec. VIII, as well as proposals of prospective physical applications. The Appendix collects the WKB approach used in Sec. II B.

II. A TWO-DIMENSIONAL MINISUPERSPACE MODEL

In this section, we study a prototype minisuperspace model that traces back to [9–11], which is described by the minisuperspace action

$$S = \mathrm{Vol}_3 \int \mathrm{d}t M(t)\left\{\mathsf{s}\left(-\frac{3}{\varkappa}\frac{\dot{\gamma}^2}{M(t)^2}+\frac{\mathsf{l}}{2}\frac{\dot{\chi}^2}{M(t)^2}\right)-V\mathrm{e}^{q\chi}\right\} \tag{1a}$$

$$=: \int \mathrm{d}t\left\{\frac{1}{2M(t)}\mathcal{G}_{IJ}q^I q^J - M(t)\mathcal{V}(q)\right\}, \tag{1b}$$

where $\mathsf{s}^2=\mathsf{l}^2=\mathsf{v}^2=1$ are signs, $\mathsf{v}:=\mathrm{sgn}V$, $q>0$ is a coupling factor, $\mathcal{G}_{IJ}$s are the components of the inverse minisuperspace DeWitt metric [1], $\mathcal{V}$ the potential, and q^I denotes collectively the minisuperspace variables $\{\gamma,\chi\}$ in configuration space. One sees that M corresponds to a lapse function and has no dynamics, whereas γ and χ are the dynamic variables.

This prototype model contains several homogeneous cosmological models as its special cases, including the closed Friedmann–Lemaître model with a free scalar field [[1], Sec. 8.1.2], the flat Friedmann–Lemaître model with a Liouville scalar field [9], and the vacuum Kantowski–Sachs model. Moreover, it is exactly solvable at both the classical and the quantum levels, which facilitates the further study of the model.

At the classical level, the trajectory in the minisuperspace spanned by (γ,χ) has a uniform representation

TABLE I. Four cases of the trigonometrical function in Eq. (2). The first case $(-,-)$ does not leave a real and physical trajectory for (γ,χ); $(-,+)$ gives infinitely many isolated trajectories due to the periodicity of the sine function, $(+,-)$ gives two, and $(+,+)$ gives one.

(l,sv)	$\mathrm{trig}\left(\sqrt{\frac{3}{2\varkappa}}g(\gamma-\gamma_0)\right)^2$
$(-,-)$	$-\sin\left(\sqrt{\frac{3}{2\varkappa}}g(\gamma-\gamma_0)\right)^2$
$(-,+)$	$\sin\left(\sqrt{\frac{3}{2\varkappa}}g(\gamma-\gamma_0)\right)^2$
$(+,-)$	$\sinh\left(\sqrt{\frac{3}{2\varkappa}}g(\gamma-\gamma_0)\right)^2$
$(+,+)$	$\cosh\left(\sqrt{\frac{3}{2\varkappa}}g(\gamma-\gamma_0)\right)^2$

$$\mathrm{e}^{q\chi}\mathrm{trig}\left(\sqrt{\frac{3}{2\varkappa}}g(\gamma-\gamma_0)\right)^2=\frac{\varkappa p_\gamma^2}{12\mathrm{Vol}_3^2|V|}, \tag{2}$$

where γ_0 is a constant and trig is a trigonometric function which depends on the four possible signs (l,sv); see Table I.

At the quantum level, the dynamics of cosmology are governed by the Wheeler–DeWitt equation [12],

$$0=H_\perp\left(\gamma,\chi,\frac{\hbar}{\mathsf{i}}\partial_\gamma,\frac{\hbar}{\mathsf{i}}\partial_\chi,\right)\psi(\gamma,\chi) \tag{3a}$$

$$=\left[\mathsf{s}\frac{\hbar^2}{\mathrm{Vol}_3}\left(+\frac{\varkappa}{12}\partial_\gamma^2-\frac{\mathsf{l}}{2}\partial_\chi^2\right)+\mathrm{Vol}_3 V\mathrm{e}^{q\chi}\right]\psi(\gamma,\chi), \tag{3b}$$

which provides a naive solution

$$\psi\propto \mathrm{e}^{\frac{\mathsf{i}}{\hbar}p_\gamma\gamma}\mathrm{Bessel}_{|\nu|}(x), \quad \text{where} \tag{4}$$

$$\nu:=\frac{1}{\hbar g}\sqrt{\frac{2\varkappa}{3}}p_\gamma, \qquad x:=2\sqrt{2}\frac{\mathrm{Vol}_3\sqrt{|V|}}{\hbar g}\mathrm{e}^{q\chi/2}, \tag{5}$$

and $\mathrm{Bessel}_\nu(x)$ is the Bessel-type function of order ν, the type which depends on the signs (l,sv) (see Table II), where $F_{\mathsf{i}\nu}(x)$ and $G_{\mathsf{i}\nu}(x)$ are the unmodified Bessel functions adapted to purely imaginary orders, as defined in [13].

The $(\mathsf{l},\mathsf{sv})=(-,+)$ and $(+,-)$ branches are *not* essentially self-adjoint, which was discovered in [9]; a family of self-adjoint extensions is characterized by a number $a\in[0,2)$. For $(+,-)$, the spectrum is continuous, and the orthonormal eigenfunction corresponding to ν is

$$\Xi_\nu^{(a)}(y)=N_{\Xi,\nu}^{(a)}\left(F_{\mathsf{i}\nu}(x)\cos\frac{\pi a}{2}+G_{\mathsf{i}\nu}(x)\sin\frac{\pi a}{2}\right), \tag{6}$$

where $N_{\Xi,\nu}$ is the δ-normalization factor [9]. For $(-,+)$, the spectrum is *discrete* with

TABLE II. Four cases of the Bessel function in Eq. (4). Branches that diverge at the infinite boundary are in *gray*, which are to be dropped. The remaining branches are all real and have no imaginary part.

(l, sv)	$\mathrm{Bessel}_\nu(x)$
$(-,-)$	$c_1K_\nu(x)+c_2I_\nu(x)$
$(-,+)$	$c_1J_\nu(x)+c_2Y_\nu(x)$
$(+,-)$	$c_1F_{\mathrm{i}\nu}(x)+c_2G_{\mathrm{i}\nu}(x)$
$(+,+)$	$c_1K_{\mathrm{i}\nu}(x)+c_2I_{\mathrm{i}\nu}(x)$

$$\nu = 2n + a, \qquad n \in \mathbb{N}, \tag{7a}$$

and the corresponding orthonormal eigenfunctions read

$$\Phi_n^{(a)}(y) = N_{J,n} J_{2n+a}(x), \tag{7b}$$

$$(N_{J,n}^{(a)})^{-2} = \frac{1}{k(2n+a)}. \tag{7c}$$

These motivate the study of the minisuperspace model due to the potential of integrability.

A. An exact wave packet

Like the stationary Schrödinger equation in conventional quantum mechanics, the Wheeler–DeWitt equation is also a linear differential equation. For a family of mode functions $\{\psi_\nu\}$, which are complete integrals of the Wheeler–DeWitt equation, one could therefore choose an amplitude $\mathcal{A}(\nu)$ and construct a *wave packet*,

$$\Psi = \int \mathrm{d}\nu \mathcal{A}(\nu)\psi_\nu, \tag{8}$$

which is a general solution of the Wheeler–DeWitt equation, independent of any interpretations. It is scarce that an exact expression of a wave packet in minisuperspace models can be found. In this section we will study such a case.

Making use of [[14], Eq. (6.795.3)], we have

$$\int_{-\infty}^{+\infty} \mathrm{d}\nu\nu \mathrm{e}^{\mathrm{i}\nu y} K_{\mathrm{i}|\nu|}(x) = \mathrm{i}\pi x \mathrm{e}^{-x\cosh y}\sinh y, \tag{9}$$

and are able to construct the exact wave packet for the $(+,+)$ case of our prototype model in Table II,

$$\begin{aligned}\Psi_{\mathrm{lin}}(\gamma,\chi) \propto{}& \mathrm{e}^{\frac{g\chi}{2}}\sinh\left[\sqrt{\frac{3}{2\varkappa}}g(\gamma-\gamma_0)\right]\\ &\cdot\exp\left\{-\frac{2\sqrt{2}\mathrm{Vol}_3\sqrt{|V|}}{\hbar g}\right.\\ &\left.\times \mathrm{e}^{\frac{g\chi}{2}}\cosh\left[\sqrt{\frac{3}{2\varkappa}}g(\gamma-\gamma_0)\right]\right\},\end{aligned} \tag{10}$$

with an amplitude that "seems to be" $\mathcal{A}_{\mathrm{lin}}(\nu) \propto p_\gamma \propto \nu$ [cf. Eq. (5)]. This is a typical profile of the norm square $|\Psi|^2$ of a wave packet in Wheeler–DeWitt quantum cosmology, which forms a tube around some classical trajectory in the asymptotic region [see Fig. 1(a)].

One may wonder how an amplitude that is proportional to the "wave number" ν can lead to a smooth wave packet

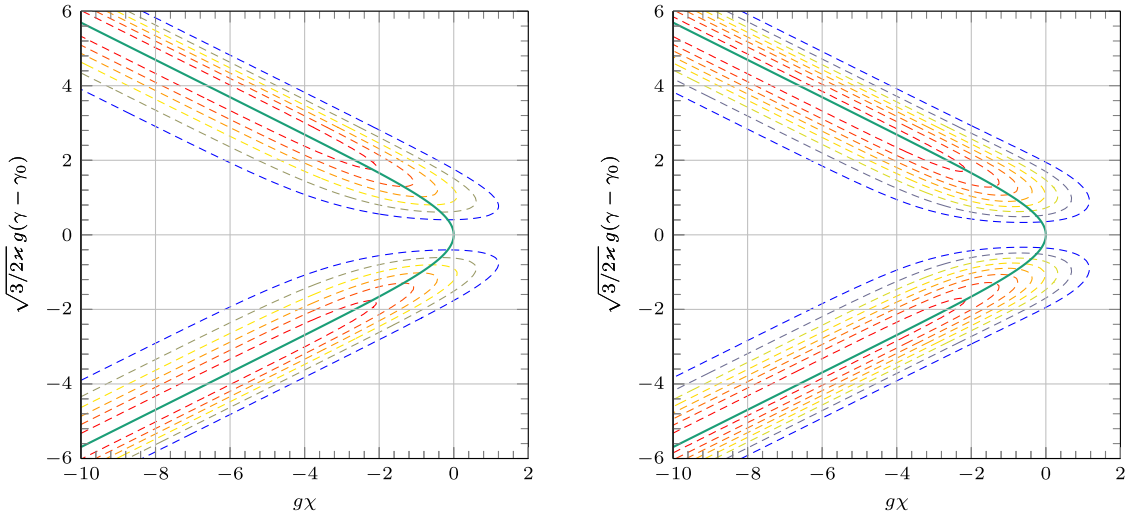

(a) $\mathcal{A}_{\mathrm{lin}}$ (b) $\mathcal{A}_{\mathrm{hfg}}$

FIG. 1. Schrödinger profile $|\Psi|^2$ of wave packets of the $(+,+)$ case of the prototype model, the mode function of which is proportional to $K_{\mathrm{i}\nu}(x)$. In Fig. 1(a), the wave packet is given by Eq. (10). The solid line is the classical trajectory with $\frac{\varkappa p_\gamma^2}{12\mathrm{Vol}_3^2|V|} = 1$, which seems to lie "on the ridge" of the wave packet. This will be studied in Sec. IV. In Fig. 1(b), a half-flipped Gaussian amplitude with respect to the normalized mode function, Eq. (16), is chosen.

that makes physical sense. For example, if one naively takes plane waves $(2\pi)^{-1/2}\mathrm{e}^{\mathrm{i}kx}$ and uses a linear amplitude, one finds

$$\frac{1}{\sqrt{2\pi}}\int_{-\infty}^{+\infty}\mathrm{d}k k\mathrm{e}^{\mathrm{i}kx} = -\mathrm{i}\sqrt{2\pi}\delta'(x), \tag{11}$$

which is 0 for $x \neq 0$.

The doubts can be dispelled if one considers the *Schrödinger normalization* of $\mathrm{i}|\nu|(x)$, which is given in [15–17], leading to the true amplitude

$$\mathcal{A}_{\mathrm{lin}}(\nu) \propto \frac{\nu}{N_{K,\nu}} \propto \sqrt{\frac{\nu}{\sinh(\nu)}}\mathrm{sgn}\nu, \tag{12}$$

where we have used a δ-normalization factor $N_{K,\nu} = k\nu\sinh(\pi\nu)/\pi^2$ for $K_{\mathrm{i}|\nu|}(x)$. In turn, the normalization condition for the amplitude $\int_{-\infty}^{+\infty}\mathrm{d}\nu|\mathcal{A}_{\mathrm{lin}}(\nu)| = 1$ gives

$$\mathcal{A}_{\mathrm{lin}}(\nu) = \sqrt{\frac{2\nu}{\sinh(\nu)}}\mathrm{sgn}\nu. \tag{13}$$

To understand more about $\mathcal{A}_{\mathrm{lin}}$, one can turn to the *Gaussian amplitude* that is popular in the literature, and compare the former with a modified version of the latter, which is flipped with respect to the x-axis for $\nu < 0$ and has the same second moment $\langle\nu^2\rangle$ as $\mathcal{A}_{\mathrm{lin}}$. The second moment for the "linear" amplitude in Eq. (13) reads

$$\int_{-\infty}^{+\infty}\mathrm{d}\nu\nu^2|\mathcal{A}_{\mathrm{lin}}(\nu)|^2 = \frac{1}{2}. \tag{14}$$

One therefore uses the *one-dimensional Gaussian distribution*

$$\mathrm{GD}_1\left(0,\sigma^2=\frac{1}{2};\nu\right) = \pi^{-1/2}\mathrm{e}^{-\nu^2} \tag{15}$$

and constructs the amplitude as

$$\mathcal{A}_{\mathrm{hfg}}(\nu) = \sqrt{\mathrm{GD}_1\left(0,\sigma^2=\frac{1}{2};\nu\right)}\mathrm{sgn}\nu = \pi^{-1/4}\mathrm{e}^{-\frac{\nu^2}{2}}\mathrm{sgn}\nu. \tag{16}$$

The corresponding wave packet, which is constructed numerically, is plotted in Fig. 1(b). One sees that it indeed resembles that with $\mathcal{A}_{\mathrm{lin}}$ in Fig. 1(a).

One may ask about a possible classical correspondence of this wave packet, which many other wave packets do have. Generally speaking, the familiar scenario would be that the wave packet is constructed by superposing mode functions with quantum number $\nu \in \mathbb{R}$ by a normal Gaussian amplitude, that is centered at ν_0. Then the claim is that this wave packet corresponds to the classical trajectory with a classical first integral $\propto \nu$; see also [9,18]. This approach is not viable here, since the amplitude is by no means a normal Gaussian one. We will focus on the issue of digging a classical trajectory out of a generic wave packet in Sec. IV, but before that, let us revisit the traditional WKB approach to derive the classical trajectory.

B. Narrow WKB Gaussian wave packet

In this section, we study a special case, in which the wave packet is constructed by superposing the WKB mode functions with a narrow Gaussian amplitude. The mathematical result confirms the heuristic idea that such a wave packet peaks near the classical trajectory, which shares the same integral constant as the center of the Gaussian amplitude.

We begin with the two-dimensional case, Eq. (1b), so that the WKB wave function reads (see the Appendix)

$$\psi(q^1,q^2;\alpha) \approx \sqrt{D}\exp\left[\frac{\mathrm{i}}{\hbar}(S(q^1,q^2;\alpha)-\alpha\beta)\right], \tag{17}$$

where the additional phase $\alpha\beta$ will soon become clear. The Gaussian wave packet is the result of

$$\Psi(q^1,q^2;\alpha,\sigma) = \int \mathrm{d}A\psi(q^1,q^2;A)\mathrm{GD}_1(\alpha,\sigma^2;A)^{1/2}, \tag{18a}$$

$$\mathrm{GD}_1(\alpha,\sigma^2;A) \coloneqq \frac{\exp(-\frac{1}{2}\sigma^{-2}(A-\alpha)^2)}{\sqrt{2\pi\sigma^2}}. \tag{18b}$$

Applying Taylor's theorem to the exponent of the integrand in Eq. (18a) with respect to A at α gives

$$\psi(q^1,q^2;A)\mathrm{GD}_1(\alpha,\sigma;A)^{1/2} = \exp\left[\mathrm{i}d_1^{(0)} + \mathrm{i}(A-\alpha)d_1^{(1)} - \frac{1}{2}(A-\alpha)^2 d_1^{(2)}\right]g(A), \tag{19}$$

where

$$d_1^{(0)} \coloneqq \frac{1}{\hbar}(S(q^1,q^2;\alpha)-\alpha\beta), \tag{20a}$$

$$d_1^{(1)} \coloneqq \frac{1}{\hbar}(\partial_\alpha S - \beta), \tag{20b}$$

$$d_1^{(2)} \coloneqq \frac{1}{2}\sigma^{-2} - \frac{\mathrm{i}}{\hbar}\partial_\alpha^2 S; \tag{20c}$$

$$g(A) \coloneqq \sqrt{D}\exp(h(A)(A-\alpha)^2), \qquad h(\alpha) = 0. \tag{20d}$$

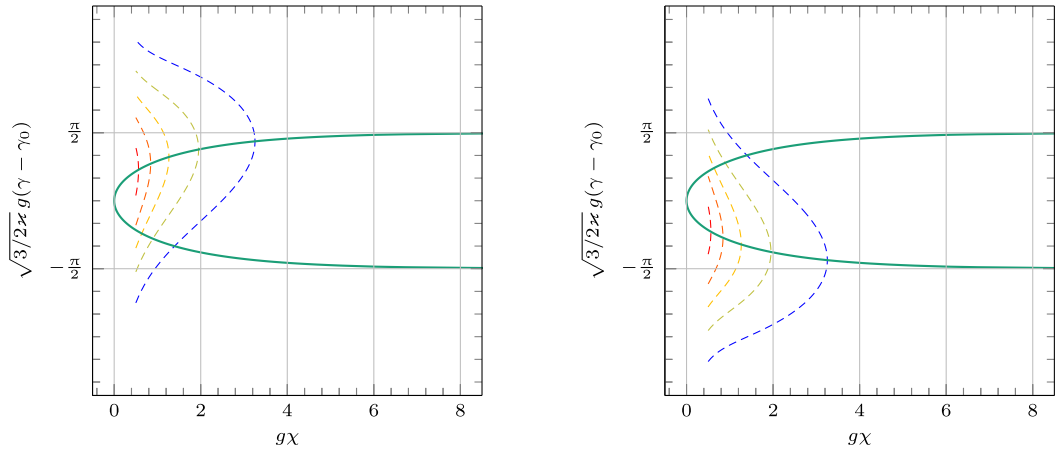

(a) $(-,+)$ with S_+ (b) $(-,+)$ with S_-

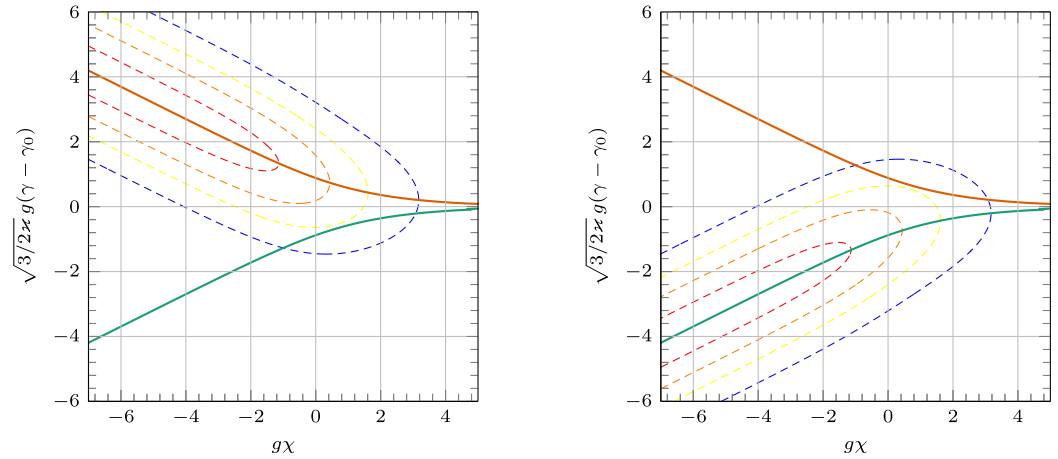

(c) $(+,-)$ with S_+ (d) $(+,-)$ with S_-

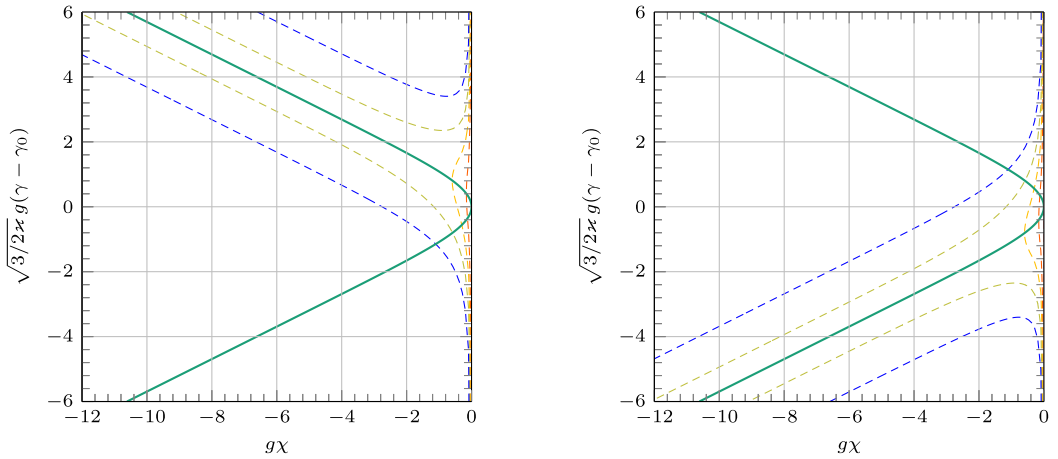

(e) $(+,+)$ with S_+ (f) $(+,+)$ with S_-

FIG. 2. Narrow Gaussian wave packets of the WKB mode functions with $S_\pm$ by Eq. (22) as dashed contours, the expressions of which are listed in Table III. One sees that for each $S_\pm$, the wave packet peaks around one asymptotic branch of the classical trajectory, which fails to hold near the turning point. Moreover, for the $(+,-)$ and $(+,+)$ cases, where $g\chi \to -\infty$ is a region in which the corresponding Bessel functions are sinusoidal, the wave packets form uniform tubes near the classical trajectory. For the $(-,+)$ and $(+,-)$ cases, where $g\chi \to +\infty$ is a region in which the corresponding Bessel functions decay exponentially in amplitude, the wave packets also decay.

TABLE III. Narrow Gaussian wave packet of the WKB mode functions with $S_\pm$ by Eq. (22), which are plotted in Fig. 2.

(l, sv)	$\sqrt{2\pi}\frac{D}{\sigma\lvert d_1^{(2)}\rvert}\cdot\exp\left[-\frac{\mathrm{Re}\, d_1^{(2)}}{\lvert d_1^{(2)}\rvert}(d_1^{(1)})^2\right]$
$(-,-)$	No solution
$(-,+)$	$\frac{2\sqrt{2\pi}\sigma}{\sqrt{+x^2-\nu^2+4\sigma^4}}\cdot\exp\left[-\frac{\sigma^2(+x^2-\nu^2)}{x^2-\nu^2+4\sigma^4}\left(\sqrt{\frac{3}{2x}}g(\gamma-\gamma_0)\mp\arccos\frac{\nu}{x}\right)^2\right]$
$(+,-)$	$\frac{2\sqrt{2\pi}\sigma}{\sqrt{+x^2+\nu^2+4\sigma^4}}\cdot\exp\left[-\frac{\sigma^2(+x^2+\nu^2)}{x^2+\nu^2+4\sigma^4}\left(\sqrt{\frac{3}{2x}}g(\gamma-\gamma_0)\mp\mathrm{arsinh}\frac{\nu}{x}\right)^2\right]$
$(+,+)$	$\frac{2\sqrt{2\pi}\sigma}{\sqrt{-x^2+\nu^2+4\sigma^4}}\cdot\exp\left[-\frac{\sigma^2(-x^2+\nu^2)}{x^2+\nu^2+4\sigma^4}\left(\sqrt{\frac{3}{2x}}g(\gamma-\gamma_0)\mp\mathrm{arcosh}\frac{\nu}{x}\right)^2\right]$

If $d_1^{(2)}$ dominates in Eq. (19), i.e., $|d_1^{(2)}|\gg 1$, the integral in Eq. (18a) can be estimated by the *stationary phase method* [3,9]. This can be realized if $\sigma^{-2}\gg\hbar^{-1}\partial_\alpha^2 S$, which means that the wave packet is constructed to be *narrow*. The result is

$$\Psi(q^1,q^2;\alpha,\sigma)\approx(2\pi)^{1/4}\left(\frac{D}{\sigma d_1^{(2)}}\right)^{1/2}\exp\left[\mathrm{i}d_1^{(0)}-\frac{(d_1^{(1)})^2}{2d_1^{(2)}}\right], \tag{21}$$

and the corresponding Schrödinger density reads

$$\begin{aligned}\rho&=\rho(q^1,q^2;\alpha,\sigma)=|\Psi|^2\\&=\sqrt{2\pi}\frac{D}{\sigma|d_1^{(2)}|}\exp\left[-\frac{\mathrm{Re}\, d_1^{(2)}}{|d_1^{(2)}|^2}(d_1^{(1)})^2\right].\end{aligned} \tag{22}$$

Given that D, $d_1^{(2)}$, and $\mathrm{Re}\,(d_1^{(2)})$ vary slowly with respect to (q^1,q^2), the peak of ρ dominates near $d_1^{(1)}=0$, i.e., $\partial_\alpha S=\beta$ [cf. Eq. (A16b)], which is just the classical trajectory. Narrow Gaussian wave packets of $(-,+)$, $(+,-)$, and $(+,+)$ cases are summarized in Table III and plotted in Fig. 2.

The above result in two dimensions can easily be generalized to higher dimensions. Consider the WKB mode function

$$\psi(q^i;\alpha_k)\approx\sqrt{D}\exp\left[\frac{\mathrm{i}}{\hbar}\left(S(q^1\ldots q^n;\alpha_1\ldots\alpha_m)-\sum_{k=1}^m\alpha_k\beta_k\right)\right], \tag{23}$$

where $m=n-1$ is the number of integral constants.

Choosing a nondegenerate m-dimensional Gaussian amplitude leads to the Gaussian wave packet

$$\Psi(q^i;\alpha_j,\Sigma_{jk})=\int \mathrm{d}A_1\ldots\mathrm{d}A_m\psi(q^i;A_k)\mathrm{GD}_m(\alpha_k,\Sigma_{kl};A_k)^{1/2}, \tag{24a}$$

where

$$\begin{aligned}&\mathrm{GD}_m(\alpha_k,\Sigma_{kl};A_k)\\&\quad:=\frac{\exp\left[-\frac{1}{2}\sum_{k,l=1}^m(\Sigma^{-1})_{kl}(A-\alpha)_k(A-\alpha)_l\right]}{\sqrt{(2\pi)^m\det\Sigma}}\end{aligned} \tag{24b}$$

is the probability density function of the multivariate Gaussian distribution [[19], Ch. 5], $m=n-1$, and Σ is the nondegenerate, positive-definite covariance matrix. The integral in Eq. (24) can also be estimated by the stationary phase method as

$$\begin{aligned}\Psi(q^i;\alpha_k,\Sigma_{kl})\approx&\left(\frac{(2\pi)^m}{\det\Sigma}\right)^{1/4}\left(\frac{D}{\det d_m^{(2)}}\right)^{1/2}\\&\cdot\exp\left(\mathrm{i}d_m^{(0)}-\frac{1}{2}\sum_{k,l}(d_m^{(2)})_{kl}(d_m^{(1)})_k(d_m^{(1)})_l\right),\end{aligned} \tag{25}$$

where

$$d_m^{(0)}:=\frac{1}{\hbar}\left(S(q^i;\alpha^k)-\sum_{k=1}^m\alpha_k\beta_k\right), \tag{26a}$$

$$(d_m^{(1)})_k:=\frac{1}{\hbar}(\partial_{\alpha_k}S-\beta_k), \tag{26b}$$

$$(d_m^{(2)})_{kl}:=\left(\frac{1}{2}\Sigma^{-1}-\frac{\mathrm{i}}{\hbar}\mathrm{Hess}_\alpha S\right)_{kl}; \tag{26c}$$

$$(\mathrm{Hess}_\alpha S)_{kl}:=\partial_{\alpha_k}\partial_{\alpha_l}S. \tag{26d}$$

The Schrödinger density of the wave packet reads

$$\begin{aligned}\rho&=\rho(q^i,\alpha_k,\Sigma_{kl})=|\Psi|^2\\&=\sqrt{\frac{(2\pi)^m}{\det\Sigma}}\frac{D}{\det d_m^{(2)}}\exp\left[-\mathrm{Re}\left(\sum_{k,l}(d_m^{(2)})_{kl}(d_m^{(1)})_k(d_m^{(1)})_l\right)\right].\end{aligned} \tag{27}$$

The corresponding classical trajectory is $(d_m^{(1)})_k = 0$, or $\beta_k = \partial_{\alpha_k} S$, which is identical to Eq. (A16a).

Therefore, we can be confident that a classical universe is likely to emerge from a quantum wave packet constructed by a narrow Gaussian amplitude, and in regions where the WKB approximation is good. The amplitudes near the peak also seem to be constant. Departure from classical theory is expected where these conditions are violated, for example when the wave packet spreads (and becomes wider), is damped (and the amplitude becomes smaller), or near the classical turning point (and the WKB approximation fails).

The idea of the "peak" of a wave packet, which was used in Eqs. (22) and (27), is heuristic. If a wave packet does not have a form as in Eqs. (22) and (27), the heuristic idea does not easily apply, which has already happened in Eq. (10). One needs a mathematical description for this idea, which will be studied in Sec. IV. One will see that in the contour approach of ridgelines, as well as in the simple first-derivative test, the classical trajectories in Eqs. (22) and (27) can be confirmed.

III. STATIONARY WAVE PACKETS

In quantum cosmology, the usual way of constructing a wave packet is linearly superposing the complete integrals ψ_ν, containing constants ν, of the Wheeler–DeWitt equation which is comparable to the stationary Schrödinger equation in quantum mechanics,

$$H\psi_\nu = E\psi_\nu, \tag{28}$$

with the solution ψ_ν which is called the wave function of a *stationary state*, where ν is another quantum number that marks different states in a degenerate level. If one writes $H_\perp = H - E$ and fixes the energy level E, Eq. (28) becomes $H_\perp \psi_\nu = 0$, which looks identical to Eq. (3a). In this resemblance, constructing a wave packet corresponds to the superposition of degenerate stationary states in the same energy level, the result of which is also an energy eigenstate of the same level.

We will call such a quantum wave packet a *stationary wave packet*, which encompasses both conventional quantum mechanics and the Wheeler–DeWitt quantum cosmology. Relating a tentative theory of quantum gravitation to quantum mechanics can lead to analog models, which has been realized in the study of black holes [20–23] and quantum field theory in curved space-time [24,25]. For a review of analog gravitation, see [26].

On the other hand, we noticed that the Rydberg, or highly excited atom, has indeed a description of such a superposition as a wave packet [27–29]. Independent of this experimental aspect, in Sec. III A we introduce the two-dimensional hydrogen atom as a toy model, and then construct stationary wave packets in Sec. III B. Meanwhile, we discuss the choice of superposition amplitudes, arguing in favor of Gaussian, binomial and Poisson amplitudes, etc., which maximizes the entropy. In the end, we turn to the study of the classical limit, and verify the correspondence principles in Sec. III C.

A. Two-dimensional hydrogen atom

Consider a spinless nonrelativistic two-dimensional hydrogen atom, described by the action

$$S = \int \mathrm{d}t \left[\frac{m}{2}(\dot{\varrho}^2 + \varrho^2\dot{\varphi}^2) + \frac{\alpha}{\varrho}\right], \qquad \alpha > 0 \tag{29}$$

in polar coordinates (ϱ, φ). The classical trajectory can be solved in terms of the conserved energy and angular momentum (E, L) as

$$\varrho = \frac{L^2}{m\alpha + \sqrt{m(2EL^2 + m\alpha^2)}\cos(\varphi - \varphi_0)}. \tag{30}$$

For $E < 0$, the system is bounded, and the trajectory is an ellipse. Fixing $\varphi_0 = 0$, the trajectory passing through $(\varrho, \varphi) = (\varrho_0, 0)$ and (ϱ_π, π) can be worked out in terms of

$$E = -\frac{\alpha}{\varrho_0 + \varrho_\pi} < 0, \qquad L = \pm\sqrt{\frac{2m\alpha}{\varrho_0^{-1} + \varrho_\pi^{-1}}}. \tag{31}$$

Upon canonical quantization, the stationary Schrödinger equation reads

$$\left(-\frac{\hbar^2}{2m}\nabla^2 - \frac{\alpha}{\varrho}\right)\psi(\varrho, \varphi) = E\psi(\varrho, \varphi), \tag{32}$$

where the Laplace–Beltrami operator,

$$\nabla^2 \coloneqq \partial_\varrho^2 + \varrho^{-1}\partial_\varrho - \frac{1}{\hbar^2\varrho^2}L^2, \qquad L \coloneqq -\mathrm{i}\hbar\partial_\varphi \tag{33}$$

is chosen. The stationary wave functions, with definite main and angular quantum numbers, are

$$\psi_{nl}(\xi, \varphi) = P_{nl}(\xi)\Phi_l(\varphi), \tag{34a}$$

$$P_{nl}(\xi) = N_{nl}\xi^{|l|}\mathrm{e}^{-\xi/2}G_{nl}(\xi), \tag{34b}$$

$$N_{nl} = \frac{1}{(2|l|)!}\left(\frac{(n + |l|)!}{(2n + 1)(n - |l|)!}\right)^{1/2}, \tag{34c}$$

$$\Phi_l(\varphi) = (2\pi)^{-1/2}\mathrm{e}^{\mathrm{i}l\varphi}, \qquad l = 0, \pm1, \pm2, \ldots, \tag{34d}$$

where

$$\xi \coloneqq \beta_n\varrho, \qquad \beta_n \coloneqq \frac{2m\alpha}{\hbar^2}\left(n + \frac{1}{2}\right)^{-1} \tag{34e}$$

are the *dimensionless radial coordinates*, and G_{nl} can be given in terms of a Kummer's [30] confluent hypergeometric function [[31], Sec. 13.2], Sonin's [[32], Sec. 40] associated Laguerre polynomial [[31], Eq. (18.11.2)], or a Whittaker function [[31], Eq. (13.14.4)] as

$$G(\xi) = {}_1F_1(|l|-n, 2|l|+1, \xi) N_{nl} \tag{35a}$$

$$= L_\mu^{(a)}(\xi) \tfrac{a!}{(\mu+1)_{2|l|}} N_{nl} \quad a = 2|l|, \quad \mu = n-|l|; \tag{35b}$$

$$= M_{\nu,|l|}(\xi)\xi^{-|l|}\mathrm{e}^{\xi/2} N_{nl} \qquad \nu = n+\tfrac{1}{2}, \tag{35c}$$

where $(a)_n \coloneqq a(a-1)\ldots(a-n+1)$ is the Pochhammer's [33] symbol [[31], Sec. 5.2(iii)]. Note that Eq. (34c) is chosen such that Eq. (34a) is normalized with respect to ξ, rather than ϱ. The energy levels for the bounded states are

$$E_n \coloneqq -\frac{m\alpha^2}{2\hbar^2}\left(n+\frac{1}{2}\right)^{-2}. \tag{36}$$

The normalization condition for scattering states $E \geq 0$ does not lead to a closed-form expression for the normalization factor, see e.g., [[34], Eq. (2.28)]. For simplicity, we focus on the case $E < 0$ in the following.

B. Stationary wave packets for the hydrogen atom

For bounded states of the two-dimensional hydrogen atom in Eq. (29), one fixes E or n and chooses a probability

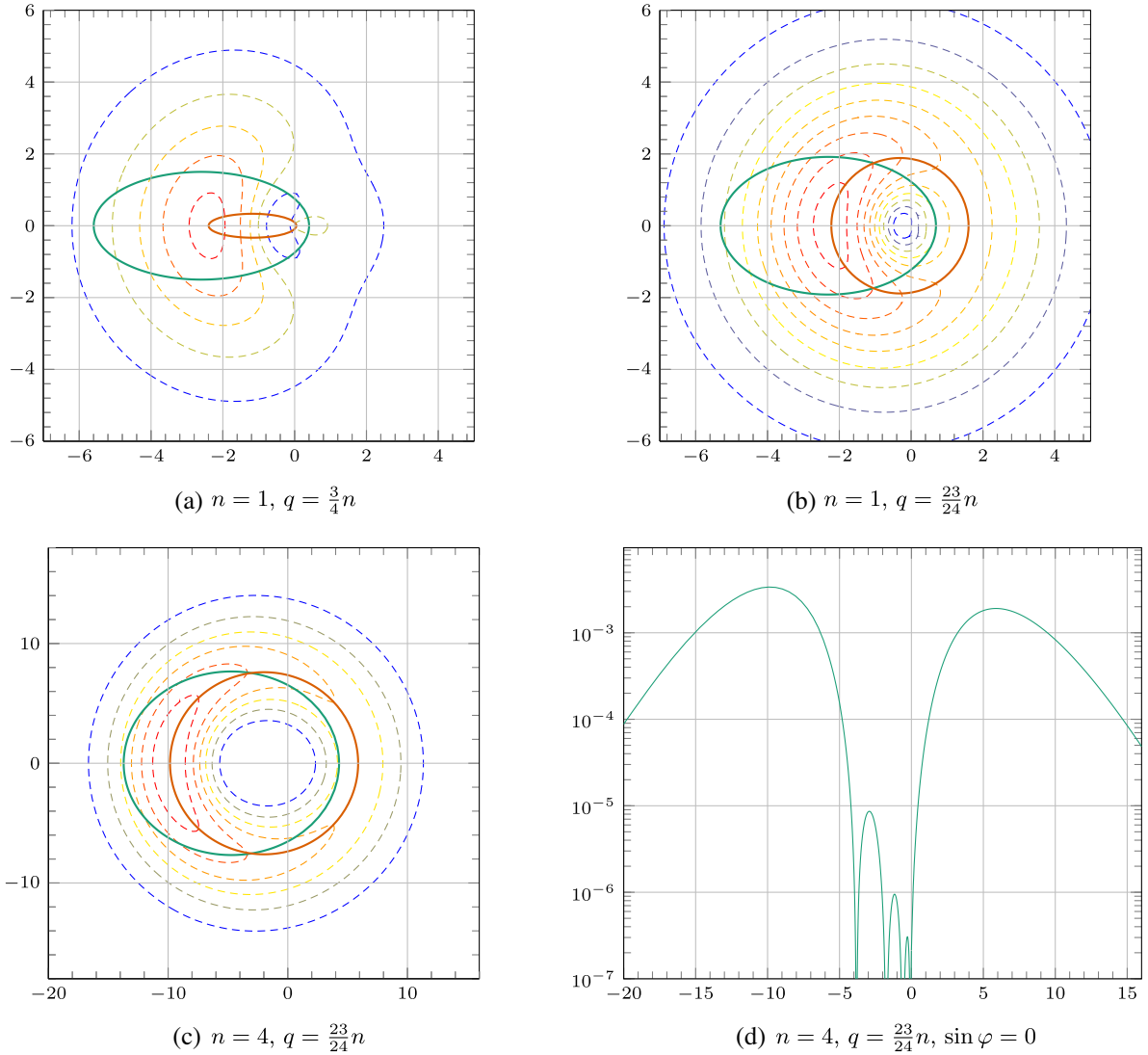

(a) $n = 1$, $q = \frac{3}{4}n$ (b) $n = 1$, $q = \frac{23}{24}n$

(c) $n = 4$, $q = \frac{23}{24}n$ (d) $n = 4$, $q = \frac{23}{24}n$, $\sin\varphi = 0$

FIG. 3. Stationary wave packets $|\Psi_{nq}(\xi,\varphi)|^2$ of the two-dimensional hydrogen atom. The green lines denote a classical trajectory in Eq. (30) with $\varphi_0 = 0$, $E = E_n$, and $L = q\hbar$. The orange lines are the classical trajectories passing through the two highest peaks of the wave packet, with the integral constants (E, L) given by Eq. (31). Apparently, the green line in Fig. 3(b) fits the orange line better than in Fig. 3(a), but worse than in Fig. 3(c). In Fig. 3(d) we show the normal projection of Fig. 3(c) on the $\sin\varphi = 0$ line (in logarithm scale). One sees that there are multiple maxima; the highest two were chosen for plotting Fig. 3(c).

amplitude for different ls to construct a stationary wave packet,

$$\Psi_{nq} \coloneqq \sum_{k=-n}^{n} A_{nk;q}\psi_{nk}. \tag{37}$$

We would like to find a choice for the $A_{nk;q}$, such that the expectation value of angular momentum

$$(\Psi_{nq}, L\Psi_{nq}) = q\hbar, \tag{38}$$

where $q \in [-n, n]$, $q \in \mathbb{R}$. Since $k \in [-n, n] \cap \mathbb{Z}$, a "natural" choice for the probability masses seems to be the *binomial distribution*, where the probability mass function is

$$\mathrm{BD}(k; u, s) \coloneqq \binom{u}{k} s^k (1-s)^{u-k}, \tag{39a}$$

$$\binom{u}{k} \coloneqq \frac{u!}{k!(u-k)!}, \tag{39b}$$

$$k = 0, 1, \ldots, u, \quad s \in [0, 1]. \tag{39c}$$

In our case, the amplitude satisfies

$$|A_{nk;q}|^2 = \mathrm{BD}\left(n+k, 2n, \frac{n+q}{2n}\right) = (2n)^{-2n}(n-q)^{n-k}(n+q)^{n+k}\binom{2n}{n+k}. \tag{40a}$$

The most naive choice,

$$A_{nk;q} = \sqrt{\mathrm{BD}\left(n+k, 2n, \frac{n+q}{2n}\right)}, \tag{40b}$$

leads to stationary wave packets that "peak around" a classical trajectory for $|q| \lesssim n$; see Fig. 3.

C. Ridgeline of a wave packet and the correspondence principles

In quantum cosmology, people argue that the ridgeline of a wave packet peaks along a classical trajectory [5]. This would be more convincing if the statement also holds for the stationary wave packets in conventional quantum mechanics.

For the binomial wave packets here, defined by Eqs. (34a), (34d), (37), and (40b), we approximate the ridge by finding the two highest peaks of the wave packet, and find the elliptic classical trajectory passing them; see Fig. 3. The approximate ridgeline is described by the integral constants $(E_{\mathrm{ar}}, L_{\mathrm{ar}})$ given by Eq. (31).

One sees that this approximation is good as n increases, which fits Bohr's correspondence principle [35], stating that the quantum system reproduces its classical behavior in the limit of large *main* quantum number n. This can be seen in Fig. 4(a), where one fixes q/n and observes the relative difference between $(E_{\mathrm{ar}}, L_{\mathrm{ar}})$, and (E_n, L) vanishes polynomially as $n \to +\infty$.

In our application, on the other hand, we are more concerned with fixed n or E_n, and varying q. In this case, the ridgeline gets closer to the classical trajectory as the

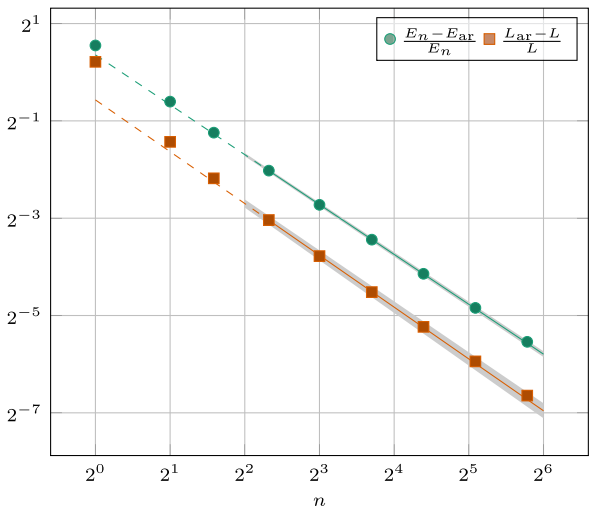

(a) Bohr's, $\frac{l}{n} \equiv \frac{23}{24}$.

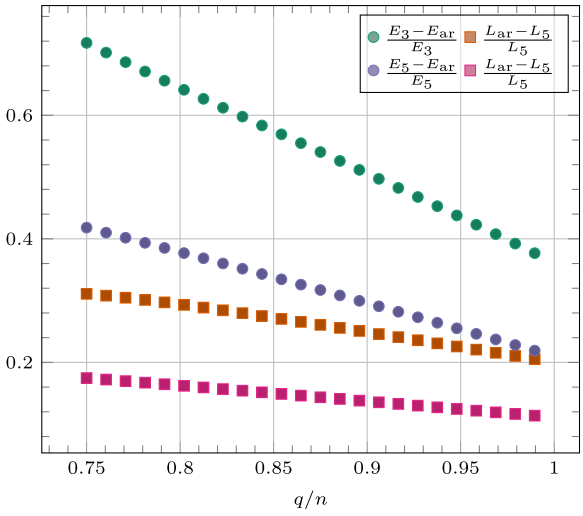

(b) Ours, $n = 3$ and 5.

FIG. 4. Correspondence principles shown in terms of the difference between $(E_{\mathrm{ar}}, L_{\mathrm{ar}})$ and $(E_n, q\hbar)$, where the former with subscript $_{\mathrm{ar}}$ denotes the integral constants that give a trajectory passing through the two highest peaks of the binomial wave packet (Fig. 3). In Fig. 4(a), the difference vanishes as $n \to +\infty$, which is accordance with Bohr. The solid line is the best fit with the generalized linear model [36] $y = g^{-1}(\beta_0 + \beta_1 \ln n)$ with $g(y) = \ln y$. In Fig. 4(b), the difference becomes smaller as $q \to n^-$, but will not vanish; this correspondence phenomenon is relevant in quantum cosmology.

effective *angular* quantum number $q \to n^-$, in the sense that the relative differences between $(E_{\rm ar}, L_{\rm ar})$ and $(E_n, q\hbar)$ become smaller in the aforementioned limit; see Fig. 4(b). The differences, however, will not vanish. This correspondence phenomenon is relevant in quantum cosmology, where the "main quantum number" is to be fixed, and only the other quantum numbers in the degenerate "energy eigenspace" can change.

IV. RIDGELINES OF WAVE PACKETS

A. The conception of ridgelines

In the remaining sections of this paper, we try to quantify the qualitative arguments in the literature—that a classical trajectory can be read off from wave packets in specific forms. Intuitively, one may imagine the profile of a wave packet as a terrain in its configuration space, where the hills and valleys are the most and least probable places to "find" the system. In physical geography, chains of mountains or hills stretch a distance, where the "highest points" form the *ridgelines*; conversely, one can define the valleys or the *dale lines* by the "lowest points."

The ridgelines and dale lines are in some senses the generalization of local maxima and minima, which are isolated points. The latter are also easier to be solved in terms of local extrema, as $\nabla\rho = 0$ as necessary but not sufficient conditions, and distinguishing them is more involved. One may give a sufficient condition when the Hessian is nonsingular, but when it is, more work needs to be done. For simplicity and clearance, we will study the ridgelines and dale lines on equal footing.

The ridgelines and dale lines have been studied by the computer scientists working on imaging and vision [37–39], where the ridge and dale lines have rich applications, especially in two-dimensional *Euclidean geometry*. In physical configuration spaces that have a higher-dimensional *(pseudo-)Riemannian geometry*, the ridge and dale lines have not been much used, to our knowledge. In addition, the Euclidean experience from computer science also needs to be thought of twice.

From now on, we will not use the analogy with terrain any further, which we argue as follows. For terrain, the altitude has the dimension of length, which is comparable to the dimension of the geographic coordinates. For a wave packet, in contrast, the dimension of its profile is *not* comparable to the dimensions of the configuration space coordinates; the former might be the inverse of the configuration volume if one has the Schrödinger normalization condition in mind,

$$\int \mathrm{dVol}|\Psi|^2 = 1, \tag{41}$$

which is *dependent* on the configuration space coordinates. Based on these considerations, we shall find an *intrinsic* description of the ridgelines of a wave packet, where the wave packet is *not* to be plotted in an additional dimension.

B. First-derivative test and Hessian matrix

Heuristically, one can simply use the first partial derivative to find the ridge and dale lines. In two dimensions with Cartesian coordinates (x, y), it reads

$$\rho_{,x} = 0 \quad \text{or} \quad \rho_{,y} = 0, \tag{42}$$

which is weaker than the extremum condition, $\rho_{,x} = 0$ *and* $\rho_{,y} = 0$.

Geometrically, Eq. (42) can be interpreted as a directional extremum test, namely to find the extremum with respect to only the x- or y-direction.

Take the "linear" wave packet in Eq. (10) as an example. With $\rho_{\rm lin} = |\Psi_{\rm lin}|^2$, the condition $\partial_\chi \rho_{\rm lin} = 0$ gives

$$\mathrm{e}^{g\chi} \cosh\left[\sqrt{\frac{3}{2\varkappa}} g(\gamma - \gamma_0)\right]^2 = \frac{g^2\hbar^2}{8\mathrm{Vol}_3^2|V|}. \tag{43}$$

Compared with Eq. (2) and Table I, Eq. (43) has exactly the form of a classical trajectory, with

$$p_\gamma^2 = \frac{3g^2\hbar^2}{2\varkappa}. \tag{44}$$

On the other hand, the condition $\partial_\gamma \rho_{\rm lin} = 0$ gives

$$\mathrm{e}^{g\chi} \cosh\left[\sqrt{\frac{3}{2\varkappa}} g(\gamma - \gamma_0)\right]^2 = \frac{g^2\hbar^2}{8\mathrm{Vol}_3^2|V|} \coth\left[\sqrt{\frac{3}{2\varkappa}} g(\gamma - \gamma_0)\right]^4. \tag{45}$$

Since $\coth\left[\sqrt{\frac{3}{2\varkappa}} g(\gamma - \gamma_0)\right] \to 1$ as $\sqrt{\frac{3}{2\varkappa}} g(\gamma - \gamma_0) \to \pm\infty$, Eq. (45) also coincides asymptotically with a classical trajectory, with the same p_γ as in Eq. (44). In contrast to Eq. (43), it has two distinct trajectories, which approach the same classical trajectory in the above-mentioned asymptotic region, while they depart from the trajectory near the classical turning point. The result is plotted in Fig. 5.

Now consider a classical trajectory that is implicitly given by an equation: $f(x, y) = 0$. This works only in two dimensions; for d-dimensions, $d > 2$, one needs $d - 1 > 1$ equations to specify an implicit curve. One can intuitively imagine a wave packet that "peaks around" this trajectory, the density of which is given by [[5], Eq. (6.3)]

$$\rho = \mathrm{e}^{-f^2}, \tag{46}$$

so that the density ρ peaks to 1 at $f = 0$, and is less than 1 for $f \neq 0$.

Using the first-derivative test with an arbitrary variable x, one has

$$0 = \partial_x \rho = -2\rho f \partial_x f, \tag{47}$$

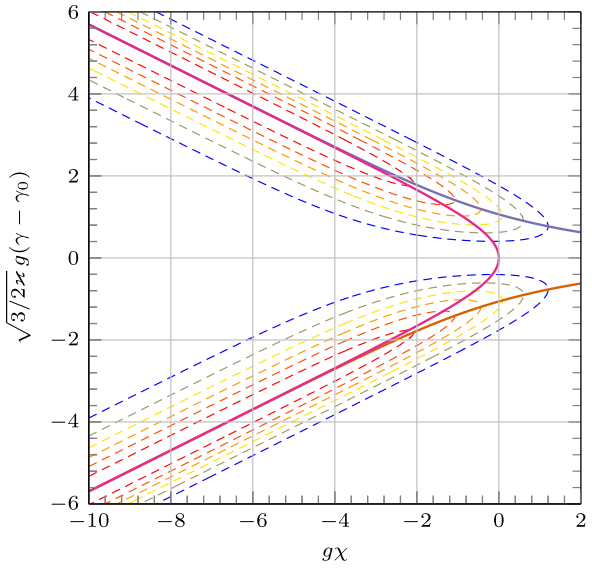

FIG. 5. The first-derivative approach shown with the "linear" wave packet in Eq. (10). The orange and purple lines are the results from Eq. (45), whereas the pink line is from Eq. (43).

and therefore

$$f = 0, \quad \text{or} \quad \partial_x f = 0. \tag{48}$$

Hence the trajectory $f = 0$ is *included* in the result of the first-derivative test.

The first-derivative test is intuitive and easy to implement. However, it is not covariant under coordinate transformation; moreover, one can construct examples where the test does not give sensible results; see Fig. 14(b). One may imagine using the eigenvector field of the Hessian $\partial_i\partial_j\rho$ as the "principle directions" and perform a directional derivative test with respect to them. This is the approach in [39].

Unfortunately, the directional derivative test is not practical in higher dimensions, where no generic expression for roots of the algebraic eigenvalue equation exists. In addition, the smoothness of the eigenvector field is difficult to establish. Moreover, upon moving to (pseudo-) Riemannian geometry, one needs to deal with the (1,1)-Hessian tensor, which is not symmetric as a matrix, and the analysis is lost in challenging calculations. We now move forward to the other two approaches of ridgelines.

V. CLASSICAL PREDICTIONS AS CONTOUR RIDGELINES

In subsection V A we first describe the ridgelines in terms of a certain character of the contour lines. One can imagine finding the *locally most curved neighborhoods* on the contour lines, the trajectory of which forms a ridge or dale line. The defining equation of this approach was first written down by Barré de Saint-Venant in 1852 [40] without derivation. We refer to [39] for a comprehensive explanation.

We will begin with the two-dimensional Euclidean case, where there are two equivalent definitions of the contour ridgelines, both of which can be generalized to higher dimensions, as well as to (pseudo-)Riemannian geometry. For the "linear" wave packet in Eq. (10), the contour approach can directly be applied.

In this subsection V B we establish a scenario with an exponential wave packet, in which the contour approach gives intuitive results. We then generalize this scenario with a slowly varying amplitude and show that an intuitive result is still contained in the result. We show how the redundant results can be identified with a toy example.

A. The contour ridgelines

1. First definition

In topography, contour lines give the altitude intrinsically. One can formulate the ridge and dale lines in terms of the contour lines, as follows [[41], Sec. 4.1]:

When representing ridges, contour lines are elongated towards ridge stretch and they are convex as they are turned towards the fall of the ridge or the ground …

Mathematically, one considers a C^2 real function $\rho(x, y)$, the contour lines γ_c of which are given by the implicit equation $\rho \equiv c$.

Having the idea of "locally most curved neighborhoods" in the introduction in mind, now let $\kappa(x, y)$ be a *characteristic function*, such that the crossing of a ridge and the contour γ_c is an extremum of κ on γ_c. This gives the first definition of a contour ridgeline, namely *the ridgeline is regarded as the locus of extrema of* κ *under the constraint* $\rho = c$.

The statement can be formulated by the method of Lagrange multipliers,

$$\mathrm{d}\rho = \lambda_c \mathrm{d}\kappa, \tag{49a}$$

$$\rho = c, \tag{49b}$$

where λ_c is the Lagrange multiplier. Equation (49a) can be separated into a system of equations in the bases $\mathrm{d}x$ and $\mathrm{d}y$. Then eliminating λ_c gives

$$0 = \rho_{,x}\kappa_{,y} - \rho_{,y}\kappa_{,x}, \tag{50}$$

where "," denotes partial derivative [[42], Eq. (2.25)].

In practice, one can use the squared norm of $\mathrm{d}\rho$ as the characteristic function

$$\kappa = \kappa_{\mathrm{sqr}}(x, y) = \rho_{,x}^2 + \rho_{,y}^2. \tag{51}$$

Substituting Eq. (51) into Eq. (50) results in the *de Saint-Venant equation for ridges* (dSVr) [37,40],

$$0 = \rho_{,x}\rho_{,y}(\rho_{,x,x} - \rho_{,y,y}) - (\rho_{,x}^2 - \rho_{,y}^2)\rho_{,x,y}. \tag{52}$$

2. Second definition

To see the mathematical structure more clearly, we use the generalization of Eq. (51) in Eq. (55). Substituting the latter in Eq. (49a) gives the tensorial equation

$$\rho_{;i} = 2\lambda_c \rho_{;i}{}^{;j} \rho_{;j}. \tag{53}$$

In other words, $\rho^{;i}$ is an eigenvector of its Hessian $\rho^{;i}{}_{;j}$. This gives the second characteristic of a contour ridgeline: it is *the locus of points where the gradient is an eigenvector of the Hessian*.

3. Generalizations

The results above in two dimensions can easily be generalized to higher-dimensional (pseudo-)Riemannian spaces. From Eq. (49a) one can derive

$$0 = \mathrm{d}\rho \wedge \mathrm{d}\kappa, \tag{54}$$

which takes the place of Eq. (50). For Eq. (51), the generic version reads

$$\kappa_{\mathrm{sqr}} = \star^{-1}(\mathrm{d}\rho \wedge \star \mathrm{d}\rho) = \mathrm{d}\rho^{\sharp} \lrcorner \, \mathrm{d}\rho = g^{ij}\rho_{;i}\rho_{;j}, \tag{55}$$

where $\star$ is the Hodge star operator [[43], Sec. 28], $^{\sharp}$ is a musical isomorphism, $\lrcorner$ is the interior product or contraction [[43], Sec. 23], g^{ij} is the inverse metric, and the symbol; denotes the covariant derivative with respect to an affine connection [[44], Sec. 85].

Inserting Eq. (55) in Eq. (54) gives the *covariant dSVr equation*

$$0 = \mathrm{d}\rho \wedge \mathrm{d}(\mathrm{d}\rho^{\sharp} \lrcorner \, \mathrm{d}\rho). \tag{56}$$

This equation is to be understood as imposing all its components to be zero, and therefore defining an *implicit* curve.

4. Application to the "linear" wave packet

The contour approach can immediately be applied to the "linear" wave packet in Eq. (10). Using the DeWitt metric in Eq. (1b), the de Saint-Venant equations for ridges (56) can be factorized such that

$$0 = y, \quad \text{or} \tag{57a}$$

$$0 = x^3 \sinh(y)^4 - x^2 \cosh(y) \sinh(y)^2 - x \cosh(y)^2 + \cosh(y), \tag{57b}$$

where $x > 0$ is given in Eq. (5), $y = \sqrt{\frac{3}{2\varkappa}} g(\gamma - \gamma_0)$. One can solve x from Eq. (57b) in terms of y,

$$3x_k = 1 + 4\cos\left[\times \frac{2k\pi + \arctan[19 - 8\cosh(2y), 3\sqrt{48\cosh(2y) - 33}]}{3}\right], \quad k = 0, 1, 2, \tag{58}$$

where $\arctan(x, y)$ gives $\varphi \in [0, 2\pi)$ such that $\cos\varphi = \frac{x}{\sqrt{x^2+y^2}}$, $\sin\varphi = \frac{y}{\sqrt{x^2+y^2}}$.

In Eq. (58), since

$$\lim_{y\to\infty} \arctan[19 - 8\cosh(2y), 3\sqrt{48\cosh(2y) - 33}] = \pi, \tag{59}$$

one obtains

$$\lim_{y\to\infty} x_k = (-)^{k+1} 3. \tag{60}$$

Therefore, the cases $k = 0$ and 2 give positive x and real χ as $\chi \to \infty$, whereas $k = 1$ does not. Exact calculation shows that $x_2 < 0$ for all $y \in \mathbb{R}$, and is to be excluded.

These results are plotted in Fig. 6. One sees a redundant line $y = 0$ that is a dale, a pink line that resembles a classical trajectory, and two further solid lines that converge to the same classical trajectory as $\gamma \to \pm\infty$. Nevertheless, the deviation from classical trajectory is apparent. More precisely, the classical prediction from the ridgelines by the contour approach does not match the classical

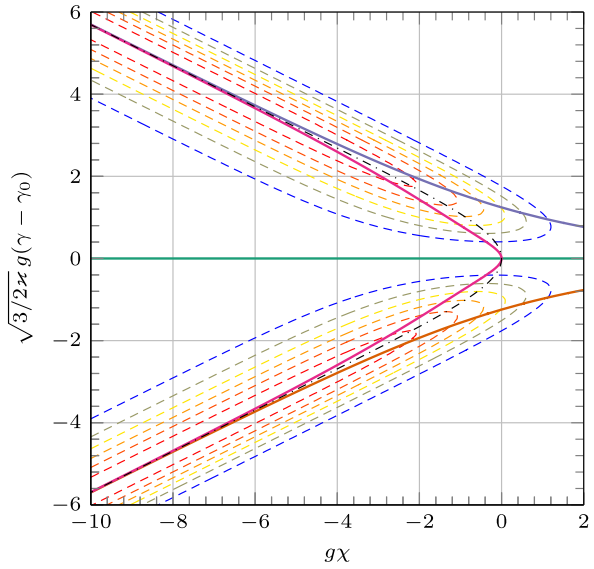

FIG. 6. The contour approach shown with the "linear" wave packet in Eq. (10). We have used the *Lorentzian* minisuperspace metric in Eq. (1b). The orange and purple lines are the results from first-derivative test, whereas the dark dash-dotted line is classical solution, Eq. (43). The pink solid line is derived by the contour approach in Eq. (58).

trajectory around the turning point, which can be regarded as quantum correction to the classical theory.

5. Curvature as the characteristic function

In two dimensions, it is tempting and intuitive to use the curvature of the contours as the characteristic function. We argue that this choice will not fit our purpose. Upon generalizing to higher dimensions, the curvature of an $(n-1)$-dimensional contour becomes the scalar-valued second fundamental form, which is a symmetric tensor. One may want to further analyze this tensor, and study its orthonormal eigenvectors [39].

Unfortunately, for the cases where the (DeWitt) metric is indefinite (e.g., Lorentzian), the second fundamental form is defined differently for the time- and spacelike patches [[45], Sec. 1.2.4], which discontinue at the null edge, where the second fundamental form is again defined differently [46]. The reason is that, for time- and spacelike hypersurfaces, the second fundamental form depends on the choice of a unit normal vector, which of course discontinues going from a timelike patch to a spacelike patch. Moreover, the eigenvectors of the second fundamental form may also not exist ([[45], Sec. 2.5.(2)]).

The contour ridgeline is based on first and second derivatives of ρ and always give equations for an algebraic curve. However, aside from sensible ridgelines, this approach also gives counterintuitive curves.

B. Aspects of the contour approach

1. Invariance under regular transformation and applications

For the transformation $\rho \to F \circ \rho$, the dSVr equation (56) transforms to

$$0 = \left(\frac{\mathrm{d}F}{\mathrm{d}\rho}\right)^3 \mathrm{d}\rho \wedge \mathrm{d}(\mathrm{d}\rho^\sharp \lrcorner \mathrm{d}\rho). \tag{61}$$

If F is strictly monotonic, i.e., $\mathrm{d}F/\mathrm{d}\rho \neq 0$, the extra factor is nonzero, and Eq. (61) gives the same ridgeline as Eq. (56).

Now we move back to the two-dimensional wave packet Eq. (46). Since e^x increases monotonically with respect to x, applying the above-mentioned property gives the ridgeline

$$\begin{aligned} 0 &= \mathrm{d}(f^2) \wedge \mathrm{d}(\mathrm{d}(f^2)^\sharp \lrcorner \mathrm{d}(f^2)) \\ &= 8f^3 \mathrm{d}f \wedge \mathrm{d}(\mathrm{d}f^\sharp \lrcorner \mathrm{d}f), \end{aligned} \tag{62}$$

which means

$$0 = f \quad \text{or} \tag{63a}$$

$$0 = \mathrm{d}f \wedge \mathrm{d}(\mathrm{d}f^\sharp \lrcorner \mathrm{d}f). \tag{63b}$$

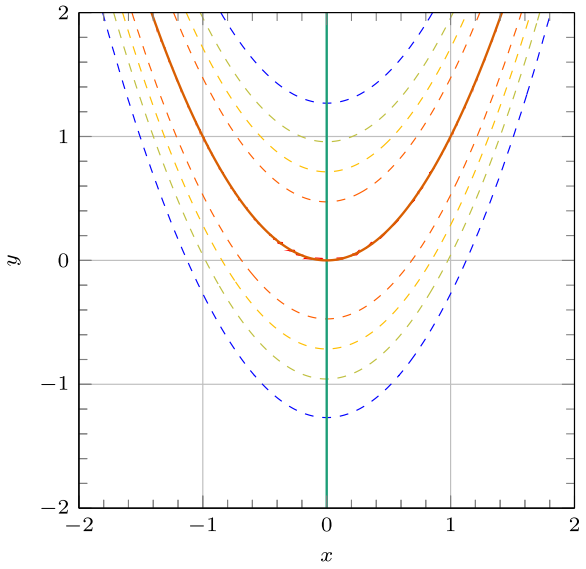

FIG. 7. Density function $\rho = \mathrm{e}^{-(y-x^2)^2}$ and the contour ridgelines, which are $x = 0$ (green, ridgeline for $y < 0$ and dale line for $y > 0$) and $y = x^2$ (orange). Incidentally, these lines are also given by the first-derivative test $\rho_{,x} = 0$, $\rho_{,y} = 0$.

Equation (63a) gives what we wanted to set up, whereas Eq. (63b) gives the ridge (or dale)line of f itself.

This is easier to see with the toy example,

$$f(x, y) = y - x^2, \tag{64}$$

so that $f = 0$ gives the parabola $y = x^2$. There is an additional solution to the dSVr equation, $x = 0$, satisfying Eq. (63b). See Fig. 7.

The parabola $y = x^2$ is what we wanted. However, we also get $x = 0$, which is a dale line for the density function $f = y - x^2$; as for $\rho = \mathrm{e}^{-f^2}$, it is a ridgeline for $y < 0$, and a dale line for $y > 0$. This line is a concrete mathematical result, although it does not fit our expectation.

2. Modulation and redundant lines

The results for the wave packet in Eq. (46) can be generalized to the narrow wave packet with varying amplitude,

$$\rho(x, y) = g(x, y)\mathrm{e}^{-\frac{f(x,y)^2}{2\sigma^2}}, \tag{65}$$

where σ is a constant, $\sigma \ll |\nabla g|$ characterizes the narrowness, and g is a modulation. Substituting Eq. (65) into Eq. (52) gives

$$0 = g^3 f^3 (p_f q_f (r_f - t_f) - (p_f^2 - q_f^2) s_f) + O(\sigma^2), \tag{66}$$

where $(p_f, \ldots, t_f)$ are the symbols with respect to f.

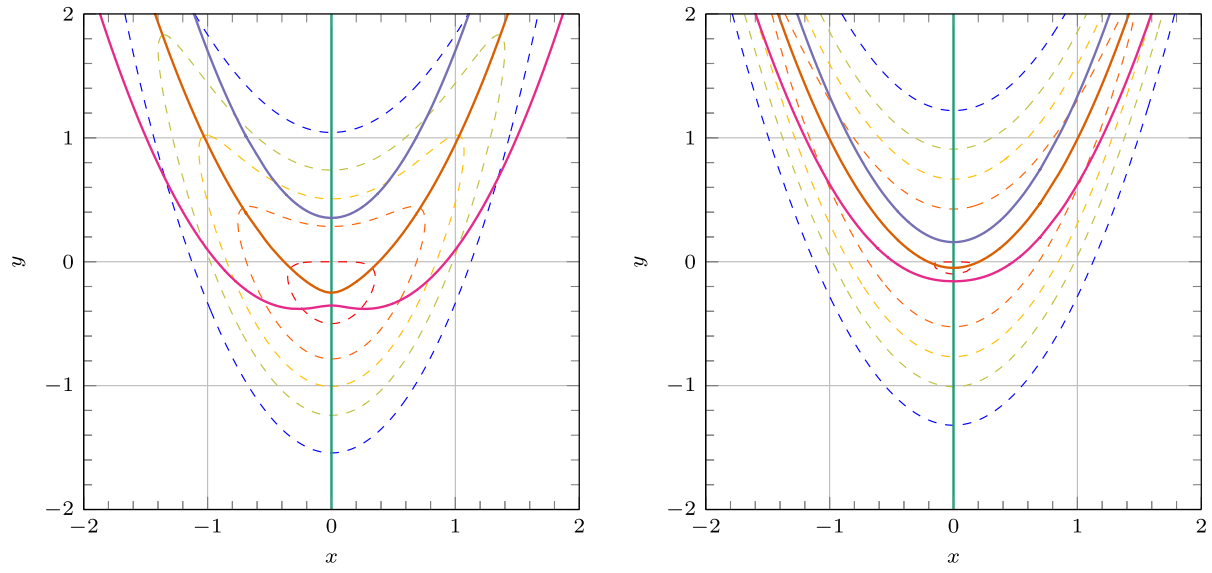

(a) $\rho = \mathrm{e}^{-(y-x^2)^2-y/2}$ (b) $\rho = \mathrm{e}^{-(y-x^2)^2-y/10}$

FIG. 8. Density function $\rho = g\mathrm{e}^{-(y-x^2)^2}$ and the contour ridgelines for $g = \mathrm{e}^{-y/2}$ and $g = \mathrm{e}^{-y/10}$ with a Euclidean metric. The green line $x = 0$ and the orange line are (qualitatively) the same as in Fig. 7; however, the dSVr equation (56) also gives the purple and the pink lines, which are apparently neither ridge nor dale lines.

As $\sigma \to 0^+$, the wave packet becomes sharper and sharper; except for an additional factor g^3, the leading-order dSVr equation recovers the case without modulation. At the limit $\sigma = 0^+$, the wave packet becomes a wall with zero width, and extends along the classical trajectory $f = 0$. Equation (66) shows that a slow modulation does not drastically change the ridgelines.

The narrow WKB Gaussian wave packets in Sec. II B is an instance of this model. The heuristic arguments we used in that section can now be replaced with the derivation in Eq. (66).

Exact calculation reveals that the approximation we used to derive Eq. (66) loses details. To see this, we also modulate Eq. (64) by

$$g = \mathrm{e}^{-2\epsilon y}, \qquad \epsilon = \frac{1}{2}, \frac{1}{10}. \tag{67}$$

The dSVr equation for $\rho = g\mathrm{e}^{-(y-x^2)^2}$, with g given in Eq. (67), reads

$$0 = 16x[-2y^3 + 2y^2(3x^2 - \epsilon) + y(-6x^4 + 8\epsilon x^2 + \epsilon) + 2x^6 - 6\epsilon x^4 - \epsilon x^2 + \epsilon^2], \tag{68}$$

which has been factorized into $x = 0$, and a term cubic in y. One can solve y in terms of x from the factor in a square bracket, where the three roots $y = y(x)$ are all real. See Fig. 8.

Only one of the three roots approaches $y = x^2$ as $x \to \infty$. This can be seen by expanding $y(x) - x^2$ at $\epsilon = 0^+$, which yields

$$y_{1,2}(x) - x^2 = \mp\sqrt{\frac{1+4x^2}{2}}\epsilon^{1/2} + \left(-1 + \frac{1}{1+4x^2}\right)\frac{\epsilon}{2} + O(\epsilon^{3/2}), \tag{69a}$$

$$y_3(x) - x^2 = -\epsilon\frac{1}{1+4x^2} + O(\epsilon^2). \tag{69b}$$

As $x \to \pm\infty$, $y_3 - x^2$ converges to 0, whereas $y_{1,2} - x^2$ diverges, and can be interpreted as the locus of the "locally flattest places on the contour," resembling $x = 0$ for $y = x^3$.

The extra curves in Eq. (69a) seem to be a common feature of the dSVr equation. Here we have managed to remove them by asymptotic analysis at infinity, recovering the intuitive result y_3. The extra line $x = 0$ has been discussed at the end of the last part.

3. Two-dimensional hydrogen atom revisited

The binomial stationary wave packets of the two-dimensional hydrogen atom, described in Sec. III, can also be studied by the contour approach. For $n = 1$, the dSVr equation is a sextic equation with respect to the dimensionless radial coordinate ξ, which has a quadratic and a quartic factor,

$$0 = -x^2(\sqrt{\ldots}\cos\varphi - 1)^2 + x(\sqrt{\ldots}^2\cos(2\varphi) + 3\sqrt{\ldots}^2 - 6\sqrt{\ldots}\cos\varphi + 2) + \sqrt{\ldots}(2\cos\varphi - 3\sqrt{\ldots}), \quad \text{or} \tag{70a}$$

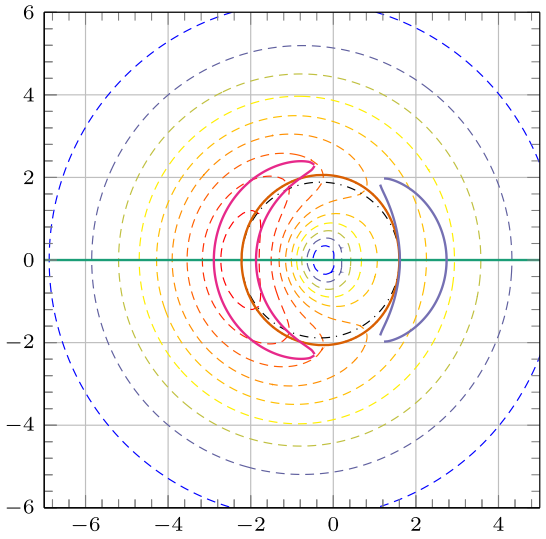

FIG. 9. Stationary wave packet $|\Psi_{1,\frac{23}{24}}(\xi,\varphi)|^2$ of the two-dimensional hydrogen atom with $n=1$, $q=\frac{23}{24}$. See Sec. III for details. The thick lines with color are solutions of the dSVr equation, whereas the dash-dotted line is the "best-fit trajectory" that crosses the maxima, adapted from the orange line in Fig. 3(b). The discontinuities within the same color are a numerical artifact.

$$\begin{aligned}0 = {}& +4x^4(\sqrt{\dots}\cos\varphi - 1)^3 + x^3[-4\sqrt{\dots}^3\cos(3\varphi) \\ & + 30\sqrt{\dots}^2\cos(2\varphi) - 4(5\sqrt{\dots}^2 + 16)\sqrt{\dots}\cos\varphi \\ & + 38\sqrt{\dots}^2 + 20] + x^2\{6\sqrt{\dots}[+2(3\sqrt{\dots}^2 + 8)\cos\varphi \\ & - 5\sqrt{\dots}\cos(2\varphi)] - 74\sqrt{\dots}^2 - 28\} + 4x[-2(3\sqrt{\dots}^2 + 4) \\ & \times\sqrt{\dots}\cos\varphi + 13\sqrt{\dots}^2 + 2] - 12\sqrt{\dots}^2, \end{aligned} \tag{70b}$$

where $\sqrt{\dots} \coloneqq \sqrt{1-q^2}$. We are therefore able to obtain solutions in terms of roots. Aside from $\sin\varphi = 0$, there are six solution $\xi = \xi(\varphi)$, three of which are real and positive near $\varphi = 0$ and $\varphi = \pi$; one is from the quadratic factor and has a simple form, while the other two are very complicated. We managed to plot them in Fig. 9.

One sees that the orange ridge given by the dSVr equation is very close to the "best-fit trajectory" that passes through the maxima of the wave packet. Like in the case $\rho = g\mathrm{e}^{-f^2}$, there are two additional lines, which might be the locally flattest points of the contours.

4. Lorentzian signature

In quantum cosmology, the minisuperspace DeWitt metric usually has a Lorentzian signature. For the Lorentzian metric

$$\mathrm{d}s^2 = -\mathrm{d}t^2 + \mathrm{d}x^2, \tag{71}$$

the Lorentzian dSVr, according to Eq. (56), reads

$$0 = -\rho_{,x}\rho_{,t}(\rho_{,x,x} + \rho_{,t,t}) + (\rho_{,x}^2 + \rho_{,t}^2)\rho_{,x,t}. \tag{72}$$

In Fig. 6, we have already shown a sensible result with contour ridgelines in a Lorentzian signature.

For the $\rho = g\mathrm{e}^{-f^2}$ model, we can also mimic the scenario by replacing $y \to t$ in Eqs. (64) and (67), and using the metric in Eq. (71). The result can still be factorized to $x = 0$ and a cubic algebraic equation with respect to t; see Fig. 10.

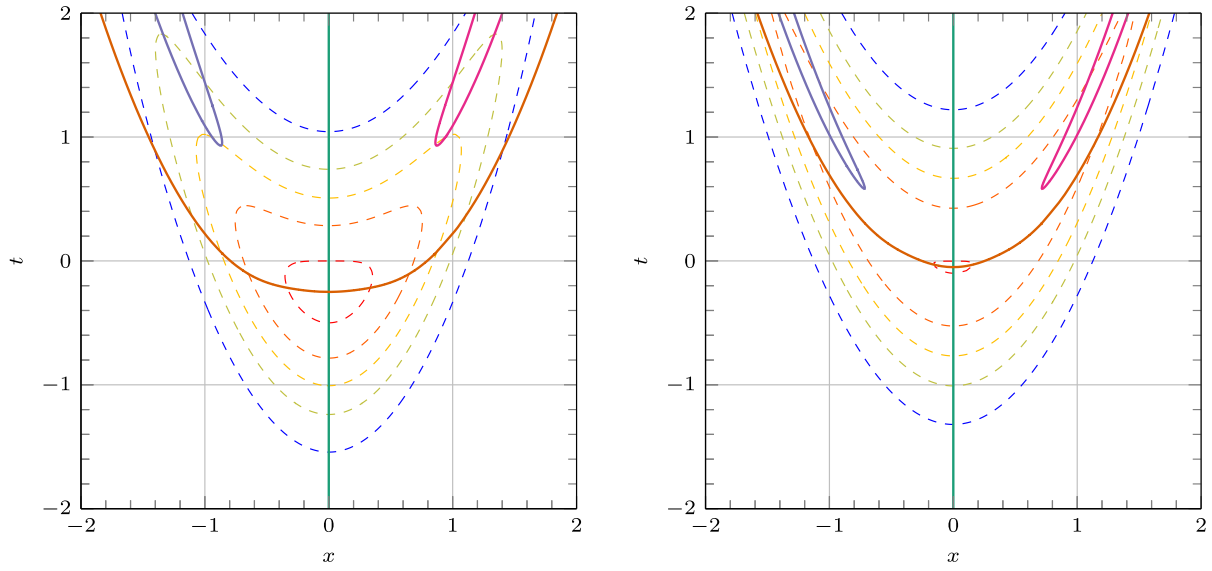

(a) $\rho = \mathrm{e}^{-(t-x^2)^2 - t/2}$ (b) $\rho = \mathrm{e}^{-(t-x^2)^2 - t/10}$

FIG. 10. Density function $\rho = g\mathrm{e}^{-(t-x^2)^2}$ and the contour ridgelines for $g = \mathrm{e}^{-t/2}$ and $g = \mathrm{e}^{-t/10}$ with an Lorentzian metric (71). The green line $x = 0$ is the same as in Figs. 7 and 8. The orange line fits intuition better near $x = 0$, whereas the other two lines both have a sharp turning point, and one of the branches fits the intuitive ridge in the asymptotic region.

Intriguingly, *none* of the three curves given by the latter factor lies on the intuitive ridge globally; instead, for the turning and asymptotic regions, there is one branch for each case that fits well with intuition.

VI. CLASSICAL PREDICTIONS AS STREAM RIDGELINES

Now we consider the ridges in terms of *singular* stream lines of the gradient vector field, which dates back to Rudolf Rothe in 1915 [47]. Heuristically, one imagines that water slowly flows from the top of a hill along the stream lines of the gradient vector field. The water stream diverges from a ridge and converges to a dale. This is the intuitive notion of the singularity of the stream lines along ridge and dale lines.

The stream approach is also adapted by modern computer scientists in image processing and computer vision [37,38]. The mathematics behind this approach is the inverse integral factor and inverse Jacobi multiplier, which work for two- and higher-dimensional cases, respectively [48,49]. We will focus on the two-dimensional case.

After a general discussion in Sec. VI A, we examine two families of density function, for which the stream ridgelines can be exactly solved in Sec. VI B. We then show that the toy model $\rho = \mathrm{e}^{-(y-x^2)^2}$ introduced in Sec. V B belongs to one of the families. In the end we investigate the cases with a Lorentzian metric signature.

A. The stream ridgelines

1. Inverse integral factor

In $\mathbb{R}^2$ with Cartesian coordinates (x, y), the contours of ρ are defined by $\mathrm{d}\rho = 0$, or $\rho = c$; dual to them are the stream lines, characterized by $\mathrm{d}w = 0$ or $w = c$, where

$$\theta \mathrm{d}w = \star \mathrm{d}\rho = -\rho_{,y}\mathrm{d}x + \rho_{,x}\mathrm{d}y, \tag{73}$$

in which θ compensates the nonintegrability of the right-hand side and is therefore called an *inverse integral factor*. One also has

$$0 = \rho_{,x}w_{,x} + \rho_{,y}w_{,y} = \star^{-1}(\mathrm{d}\rho \wedge \star \mathrm{d}w). \tag{74}$$

(θ, w) is unique up to

$$\theta \to \theta/F'(w), \qquad w \to F(w), \tag{75}$$

where $F(w)$ is an arbitrary function. One may worry that this arbitrariness renders the stream approach as not giving definite results, which fortunately does not seem to be the case; see Sec. VII.

One sees that if $\theta = 0$ and $\rho_{,x} \neq 0 \neq \rho_{,y}$ at (x_0, y_0), w cannot be expanded by the Taylor theorem at (x_0, y_0), since the linear term blows up by Eq. (73) [[47], Sec. 7]. (x_0, y_0) is said to be on a *singular stream line*.

One can imagine that if the ridge and dale lines are required also to be stream lines themselves, then the neighboring stream lines converge to the former, and diverge from the latter, along the direction of the gradient vector field. In other words, *stream ridge and dale lines are singular stream lines*. It has been shown that along these stream lines, one has [48]

$$\theta(x, y) = 0. \tag{76a}$$

The integrability condition $\mathrm{d} \wedge \mathrm{d}w = 0$, or $\theta_{,x,y} = \theta_{,y,x}$, gives the differential equation for θ,

$$\rho_{,x}\theta_{,x} + \rho_{,y}\theta_{,y} = (\rho_{,x,x} + \rho_{,y,y})\theta. \tag{76b}$$

Equations (76a) and (76b) define the stream ridge and dale lines.

2. Generalizations

The results above in two dimensions can readily be generalized to n-dimensional curved spaces. Consider local coordinates $(x^1, \ldots, x^n)$, $n \geq 2$. The gradient vector field v of ρ is given by

$$v^i\partial_i \equiv v = \mathrm{d}\rho^\sharp \coloneqq g^{ij}f_{,j}\partial_i. \tag{77}$$

One has $(n-1)$ linearly independent ws for the stream lines, satisfying

$$0 = v^i\partial_i w = v(w), \tag{78}$$

which is the generalization of Eq. (74). They are nothing else but the $(n-1)$ first integrals [50], which require $(n-1)$ inverse integral factors θ.

Similar to Eq. (73), one has for instance

$$\theta \mathrm{d}w = v^1\mathrm{d}x^j - v^j\mathrm{d}x^1, \qquad 2 \leq j \leq n, \tag{79}$$

given $v^i \neq 0, 1 \leq i \leq n$. All of the θs satisfying the linear, first-order partial differential equation

$$v^i\theta_{,i} = \theta v^i{}_{;i}, \quad \text{or} \quad v \lrcorner \mathrm{d}\theta = \theta \mathrm{d}^\dagger v^\flat, \tag{80}$$

where $\mathrm{d}^\dagger$ is the codifferential or the adjoint [[43], Sec. 29]. The solutions to Eq. (80) are called *inverse Jacobi multipliers* [49], which first appeared in [51].

For Riemannian geometry, the stream approach seems to always give sensible results, in contrast with the contour approach and the simple first-derivative test. However, the approach involves giving the *general integral* [[52], Sec. 3.1.2] of the partial differential equation, (78) or (80), which is only possible in very limited cases. Moreover, Lorentzian geometry gives rise to counter-intuitive

configurations of gradient *vector* fields, where the timelike component of the gradient one-form fields is flipped. This leaves us problems that are yet to be solved. See Secs. VII and VI B.

B. Aspects of the stream approach

1. Stream ridgelines of two function families

For density functions of the following two forms:

$$\rho(u,v) = f(f^u(u) + f^v(v)), \tag{81a}$$

$$\rho(u,v) = f(f^u(u) f^v(v)), \tag{81b}$$

with the metric

$$\begin{aligned} \mathrm{d}s_1^2 &= h(u,v)^2(\mathsf{g}\mathrm{d}u^2 + \mathrm{d}v^2), \\ \mathsf{g} &= \pm, \qquad h(u,v) > 0 \end{aligned} \tag{82}$$

the stream lines of the gradient vector field can be exactly solved. Note that for the Euclidean signature $\mathsf{g} = +$, Eq. (82) includes the bipolar, Cartesian, elliptic and planar parabolic coordinates for the flat geometry, and the stereographic coordinates for the spherical geometry, so that it is quite comprehensive. The Hodge-stars of the coordinate differentials read

$$\star \mathrm{d}u = \mathsf{g}\mathrm{d}v, \qquad \star \mathrm{d}v = -\mathrm{d}u; \tag{83}$$

one therefore gets

$$\theta \mathrm{d}w = \star \mathrm{d}\rho = -\rho_{,v}\mathrm{d}u + \mathsf{g}\rho_{,u}\mathrm{d}v. \tag{84}$$

By using Eqs. (74), (82), and (83), one obtains for Eq. (81a)

$$w = F\left(-\mathsf{g}\int^u \frac{\mathrm{d}\mu}{f^{u\prime}(\mu)} + \int^v \frac{\mathrm{d}\nu}{f^{v\prime}(\nu)}\right) \tag{85a}$$

$$\theta = -\frac{1}{F'} f' f^{u\prime}(u) f^{v\prime}(v), \tag{85b}$$

and for Eq. (81b)

$$w = F\left(-\mathsf{g}\int^u \frac{\mathrm{d}\mu}{(\ln f^u(\mu))'} + \int^v \frac{\mathrm{d}\nu}{(\ln f^v(\nu))'}\right) \tag{86a}$$

$$\theta = -\frac{1}{F'} f' f^{u\prime}(u) f^{v\prime}(v). \tag{86b}$$

Curiously, both Eqs. (85b) and (86b) include the result from the first-derivative test, $\rho_{,u} = 0$ or $\rho_{,v} = 0$.

2. Application to the toy model

The toy model $\rho = \mathrm{e}^{-(y-x^2)^2}$ in Sec. V B has the form of Eq. (81a). One can adapt the results in Eqs. (85a) and (85b) and get

$$w = F\left(\mathsf{g}y + \frac{1}{2}\ln x\right), \tag{87a}$$

$$\theta = 4\mathsf{g}\mathrm{e}^{-(y-x^2)^2} \frac{x(y-x^2)}{F'(\mathsf{g}y + \frac{1}{2}\ln x)}. \tag{87b}$$

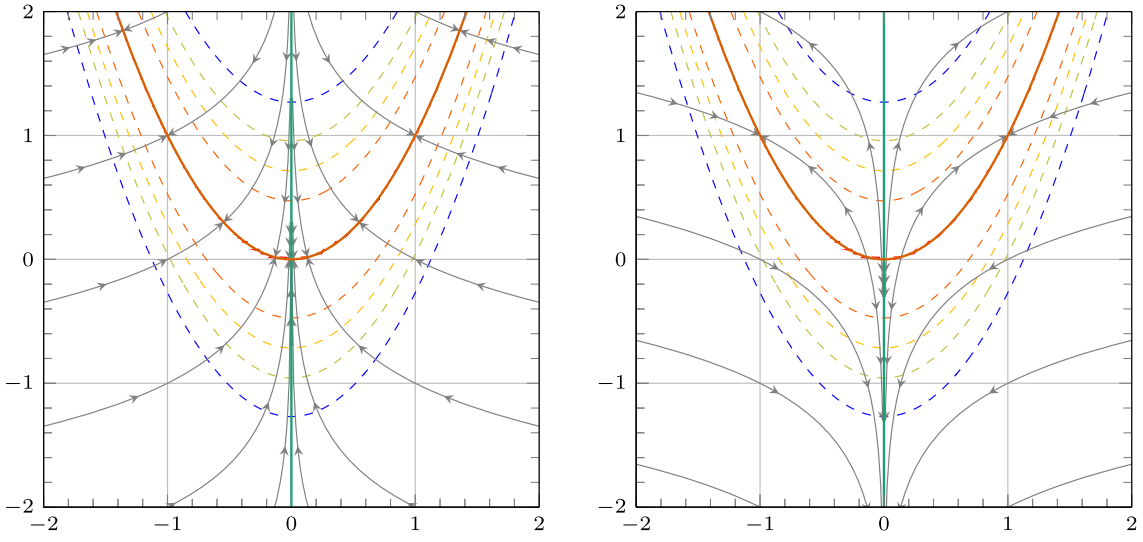

(a) Euclidean signature $\mathsf{g} = +$ (b) Lorentzian signature $\mathsf{g} = -$

FIG. 11. Density function $\rho = \mathrm{e}^{-(y-x^2)^2}$, the stream lines of the gradient vector field in both Euclidean and Lorentzian geometry, and the stream ridgelines which are $x = 0$ (green) and $y = x^2$ (orange). The Lorentzian results are to be understood with y having the negative signature in the Minkowski metric.

See Fig. 11. The Lorentzian results are to be understood with y having the negative signature in the Minkowski metric. Equation (87b) gives the same ridgelines as in the contour approach, as well as in the first-derivative test, $y = x^2$ and $x = 0$.

Now we move to the modulated toy model, $\rho = g(x,y)\mathsf{e}^{-(y-x^2)^2}$. Using $g_\epsilon = \mathsf{e}^{-2\epsilon y}$, Eq. (99) becomes

$$\mathsf{g}(-x^2 + y + \epsilon)w_{,y} + 2x(x^2 - y)w_{,x} = 0. \tag{88}$$

For $\epsilon \ll 1$, one uses the series test solution

$$w = \sum_{n=0}^{\infty} w_n \epsilon^n \quad \text{with} \quad w_0 = F\left(\mathsf{g}y + \frac{1}{2}\ln x\right), \tag{89}$$

and for $n \geq 0$,

$$(y - x^2)(2\mathsf{g}x\partial_x w_{n+1} - \partial_y w_{n+1}) = \partial_y w_n. \tag{90}$$

On the other hand,

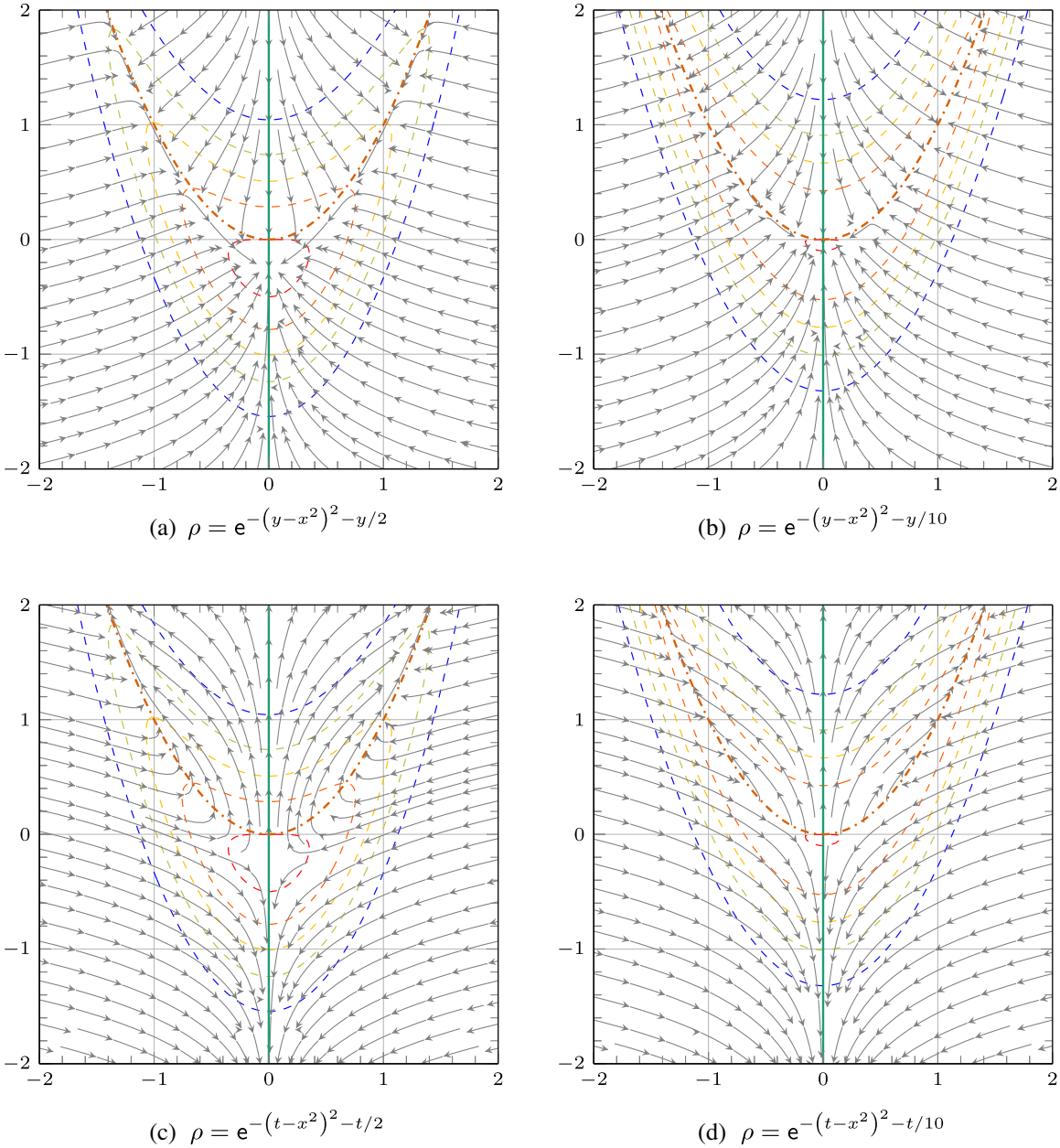

(a) $\rho = \mathsf{e}^{-\left(y-x^2\right)^2 - y/2}$ (b) $\rho = \mathsf{e}^{-\left(y-x^2\right)^2 - y/10}$

(c) $\rho = \mathsf{e}^{-\left(t-x^2\right)^2 - t/2}$ (d) $\rho = \mathsf{e}^{-\left(t-x^2\right)^2 - t/10}$

FIG. 12. Density function $\rho = g\mathsf{e}^{-(y-x^2)^2}$ and the contour ridgelines for $g = \mathsf{e}^{-y/2}$ and $g = \mathsf{e}^{-y/10}$ with the Euclidean and Lorentzian metrics. The green solid line $x = 0$ remains a ridge-dale line, whereas the orange dash-dotted line is merely an approximation in the Euclidean case; the actual singular stream lines seem to be under the orange lines. The stream ridgeline in the Lorentzian signature is apparently more intriguing.

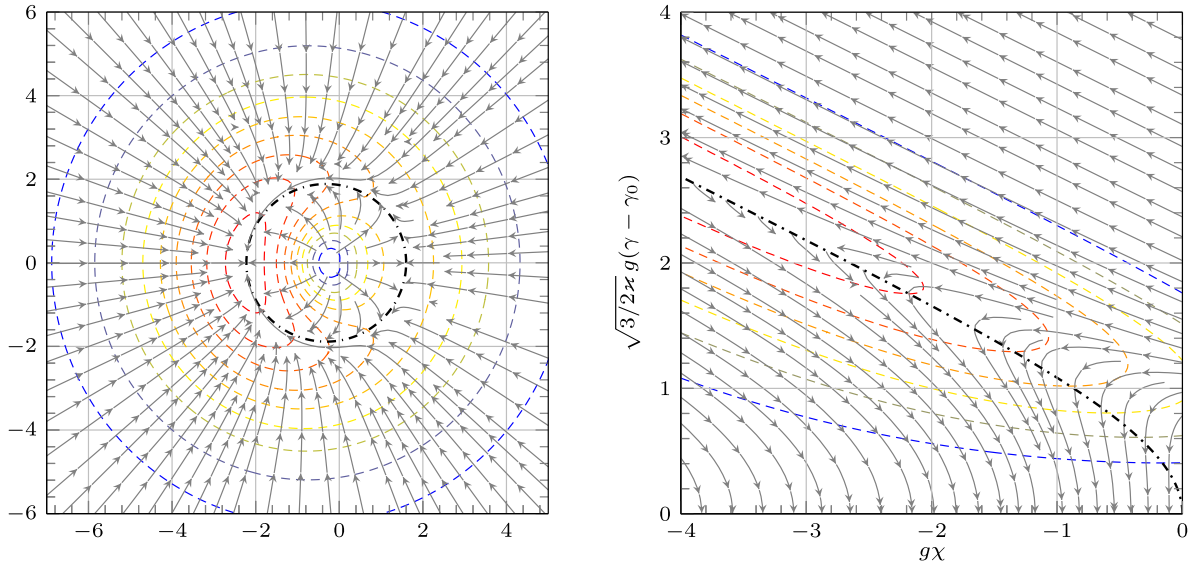

(a) 2d hydrogen atom $\Psi_{1,\frac{23}{24}}$ (b) "Linear" wave-packet

FIG. 13. (a) Numerical results of stream ridgelines for the two-dimensional hydrogen atom, and (b) the "linear" wave packet. In Fig. 13(a), the geometry is Euclidean, and the dash-dotted line is the "best-fit" classical elliptic trajectory, passing through the maxima of the stationary wave packet. In Fig. 13(b), the geometry is Lorentzian, and the dash-dotted line is the "best-fit" trajectory used before.

$$\theta = \mathsf{g}\frac{\rho_{,x}}{w_{,y}} = -\frac{\rho_{,y}}{w_{,x}}, \tag{91}$$

where ρ can also be expanded with respect to ϵ, i.e.,

$$\rho = \rho_0\left(1 + \sum_{n=0}^{+\infty}\frac{\epsilon^n}{n!}\frac{\partial^n \mathsf{e}^{-2\epsilon y}}{\partial\epsilon^n}\bigg|_{\epsilon=0}\right), \qquad \rho_0 = \mathsf{e}^{-(y-x^2)^2}. \tag{92}$$

This implies that $\theta \propto \partial_x\rho_0 \propto x(y-x^2)$.

We failed to obtain a general integral w for the modulated toy model $\rho = g\mathsf{e}^{-(y-x^2)^2}$. Numerically integrated stream lines of the gradient vector field are plotted in Fig. 12. One sees that for the Euclidean signature, the stream lines indicate the fastest uphill direction, in which the singular stream lines are ridge or dale lines that fit the intuition. Moreover, the dash-dotted orange line $y = x^2$ is a good approximation of the actual ridgeline for small ϵ (Fig. 12), but fails for larger ϵ [Fig. 12(a)]; in other words, there are nonperturbative effects that cannot be revealed by the perturbative analysis above.

With the Lorentzian signature shown in Figs. 12(c) and 12(d), things become more complicated. The above-mentioned property, that the gradient vector field points to the uphill direction, is lost. Furthermore, the apparent ridge in the plot is no longer accompanied by a possible singular stream line; instead, on the plot one sees a series of turning points that could play the role of indicating a ridgeline that also fits human cognition.

3. Numerical applications to other models

As mentioned before, it is difficult to obtain analytic results with the stream approach. For the two-dimensional hydrogen atom and the "linear" wave packet that were studied before, we make numeric plots of the stream lines of the gradient vector fields; see Fig. 13.

One sees again the good quality in the case with a Euclidean signature in Fig. 13(a), that no counterintuitive lines are present. There seems to be a singular stream line that is very close to the "best-fit" classical trajectory. For the Lorentzian geometry, the "best-fit" classical trajectory lies again near the "turning points" of the stream lines, instead of being near a singular stream line.

VII. RELATIONS OF THE CONTOUR AND STREAM APPROACHES

In this section we compare the contour and stream approaches, as well as argue against the first-derivative test. Much of the material is adapted from [37,47].

The contour and stream ridgelines can be derived on the same footing. In $\mathbb{R}^2$, from $\mathrm{d}\rho = \rho_{,x}\mathrm{d}x + \rho_{,y}\mathrm{d}y$, Eqs. (51) and (73), one deduces that [[47], Sec. 5]

$$\frac{1}{2}\mathrm{d}\kappa_{\mathrm{sqr}} = R\mathrm{d}\rho + \theta S\mathrm{d}w, \tag{93}$$

where

$$R := \frac{\rho_{,x}^2\rho_{,x,x} + 2\rho_{,x}\rho_{,y}\rho_{,x,y} + \rho_{,x}^2\rho_{,y,y}}{\kappa_{\mathrm{sqr}}^2}, \tag{94a}$$

$$S \coloneqq \frac{\rho_{,x}\rho_{,y}(\rho_{,x,x}-\rho_{,y,y})-(\rho_{,x}^2-\rho_{,y}^2)\rho_{,x,y}}{\kappa_{\mathrm{sqr}}^2}. \quad (94b)$$

Imposing κ_{sqr} to be stationary in the direction of w gives

$$0=\frac{1}{2}\frac{\partial\kappa_{\mathrm{sqr}}}{\partial w}=\theta S, \quad (95)$$

which gives either $\theta=0$ or $S=0$; they correspond to the contour and stream ridgelines defined in Eqs. (52) and (76a), respectively.

The contour and stream ridgelines are distinct, except for two special cases. Breton de Champ (see [[47], Sec. 2]) has shown that *stream lines* satisfying $S=0$ are *necessarily straight lines*; otherwise, contour ridgelines should not be stream lines, and they are therefore not stream ridgelines. However, it seems to us that points satisfying $\rho_{,x}=\rho_{,y}=0$ also lie on both the contour and stream ridgelines; see Secs. V B and VI B for an example.

The differences of the contour and stream ridgelines, as well as the simple first-derivative test, can be shown with a so-called two-dimensional *helicoidal gutter* [[37],

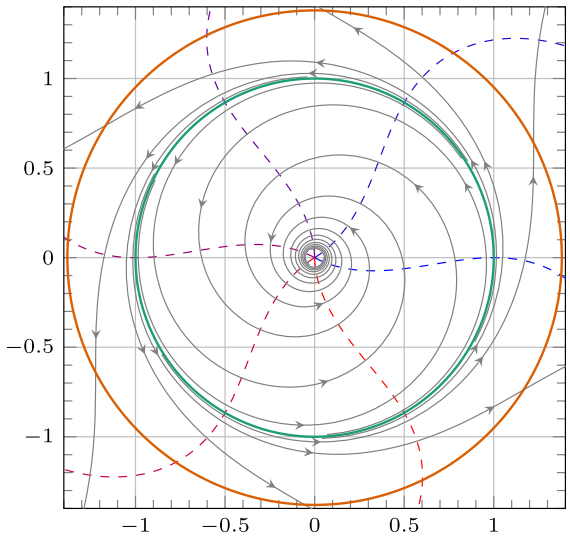

(a) Contour and stream ridge-lines

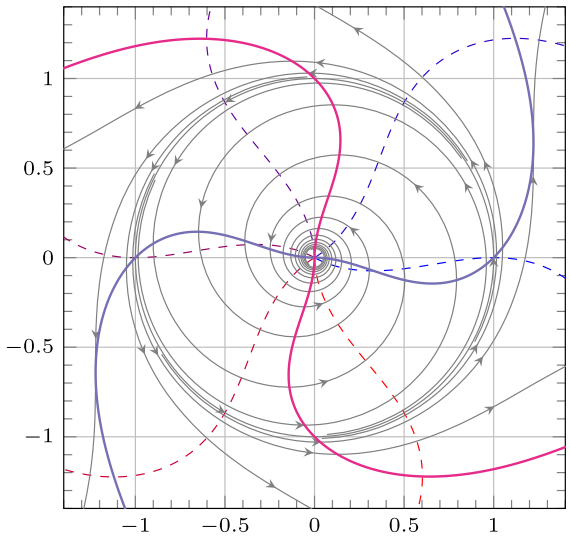

(b) First-derivative lines

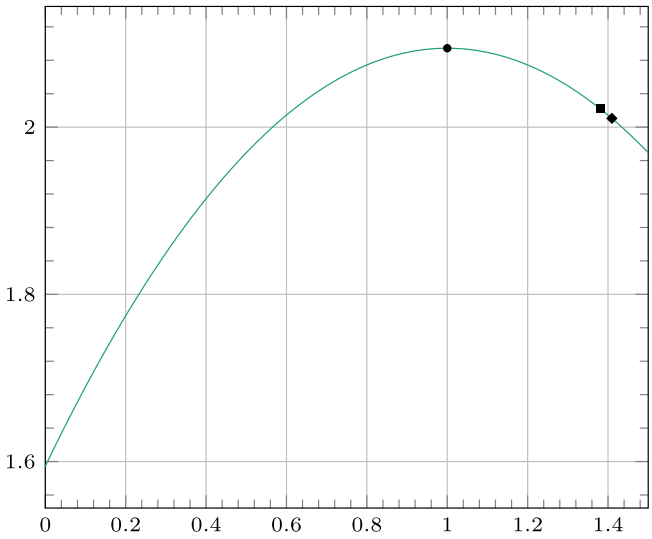

(c) Section at $\varphi=2\pi/3$

FIG. 14. The so-called helicoidal gutter in Eq. (96b), its contours (dashed lines) and gradient vector field (represented by the gray stream lines with arrows), and its ridgelines. In Fig. 14(a), the green line is the stream ridgeline given by $\theta=0$, and the orange line is the contour ridgeline predicted by the dSVr equation. In Fig. 14(b), the pink and the purple lines are $\rho_{,x}=0$ and $\rho_{,y}=0$, respectively. In Fig. 14(c), the section at $\varphi=2\pi/3$ is plotted, where the round, square, and diamond points are the stream and contour ridgelines, as well as the first-derivative line. One sees that it is the *stream ridgeline* that picks the highest point in the sense of the constant φ-section.

Sec. 6]; in polar coordinates (ϱ, φ) the metric and the gutter are

$$\mathrm{d}s^2 = g_{ij}\mathrm{d}x^i\mathrm{d}x^j = \mathrm{d}\varrho^2 + \varrho^2\mathrm{d}\varphi^2, \quad \varrho > 0, \qquad 0 \le \varphi < 2\pi; \tag{96a}$$

$$\rho(\varrho, \varphi) = \varphi + \frac{1}{2}\left(\frac{\varrho}{\varrho_0} - 1\right)^2; \tag{96b}$$

see Fig. 14.

The contour ridgelines of Eq. (96b) are given by the dSVr equation, or $S = 0$ in Eq. (94b). From the covariant expression in Eq. (56), one derives

$$0 = \left(\frac{\varrho}{\varrho_0}\right)^4 - \left(\frac{\varrho}{\varrho_0}\right)^3 - 1. \tag{97}$$

The only positive root reads

$$\frac{\varrho}{\varrho_0} \approx 1.38028. \tag{98}$$

See Fig. 14(a). Roughly speaking, it crosses the contours where the latter are curved more.

As for the stream ridgelines, using Eq. (78) yields the equation for w,

$$\mathrm{d}\rho^\sharp \lrcorner\, \mathrm{d}w = 0, \quad \text{or} \quad 0 = \rho_{,i}g^{ij}w_{,j} = \left(\frac{\varrho}{\varrho_0} - 1\right)\frac{w_{,\varrho}}{\varrho_0} + \frac{w_{,\varphi}}{\varrho^2}. \tag{99}$$

The general integral to Eq. (99) reads

$$w = F\left(-\frac{\varrho_0}{u} + \varphi - \ln\left(1 - \frac{\varrho_0}{\varrho}\right)\right), \tag{100}$$

where F is an arbitrary function; see Eq. (75). In order to obtain θ, one applies Eq. (73),

$$\theta\mathrm{d}w = \star\mathrm{d}\rho = -\frac{\rho_{,\varphi}}{\varrho}\mathrm{d}\varrho + \varrho\rho_{,\varrho}\mathrm{d}\varphi. \tag{101}$$

The result is

$$\theta = \frac{\varrho}{\varrho_0}\left(\frac{\varrho}{\varrho_0} - 1\right)\left\{F'\left(-\frac{\varrho_0}{\varrho} + \varphi - \ln\left(1 - \frac{\varrho_0}{\varrho}\right)\right)\right\}^{-1}. \tag{102}$$

The stream ridgelines are then given by $\theta = 0$, or

$$\varrho = \varrho_0. \tag{103}$$

See Fig. 14(a). One sees that the arbitrariness of w encoded in F does *not* affect the effectiveness of the stream approach. Furthermore, the stream ridgeline really marks the highest point for a constant φ-section. As a stream line by itself, the stream ridgeline is also a limit cycle [[50], Sec. 1.6.3] of the gradient vector field, and is also a watershed for two distinct families of stream lines, one spirals inwards and another outwards. The contour ridgeline, on the other hand, is close to the highest point; see Fig. 14(b).

Finally, the curves given by the first-derivative test with respect to (x, y) can also be easily worked out, see Fig. 14(b). They do not respect the rotational symmetry of ρ and is therefore not very sensible. One may argue for an alternative test with respect to (ϱ, φ), but the choice itself cannot be arbitrary and needs a mathematical description, which renders the method losing its simpleness.

VIII. SUMMARY AND OUTLOOK

In this work, we have discussed the classical predictions from the *ridgelines* of stationary wave packets in quantum theory. Our results show that the predictions from ridgelines are more abundant than the solutions solved from the classical theories; moreover, there may exist distinct deviation in the predictions from the classical solutions in a certain range of minisuperspace, which arises from the quantum behavior. This implies that the real classical trajectory should be corrected in this range.

First of all, the stationary wave packets are realized in quantum mechanics with the superposition of degenerate energy eigenstates. Such cases are illustrated by the toy model of a two-dimensional hydrogen atom. In reality, the Rydberg atom can also be described by such a superposition, providing a chance to verify the theoretical statements. Wave packets constructed by superposing solutions of the Wheeler–DeWitt equation are also formally stationary. It is imaginable to make use of this fact and use quantum systems in laboratory to simulate a quantum universe or a quantum black hole. However, one crucial difference between common quantum mechanical systems and quantum cosmology is that the latter usually has a *Lorentzian* "kinetic energy term" in the Hamiltonian constraint, whereas the former mostly have a *Euclidean* kinetic energy term. One needs to be very creative to set up a simulated quantum cosmology system in laboratory.

Second, the contour approach to ridgelines, which dates back to Barré de Saint-Venant in 1852, gives us an implicit equation (56) that can readily be plotted. It may not give results that are directionally minimal, but the difference can be small; see Fig. 14(c). The curves given by the dSVr equations are typically higher-order algebraic equations, which can at least be numerically solved. For the "linear" wave packets, as well as for narrow Gaussian WKB wave packets, this approach gives sensible results, as discussed in Sec. V and earlier in this section. With a Euclidean signature, redundant curves can appear, as we have seen in this section with the modulated toy model $\rho = g\mathrm{e}^{-f^2}$, as

well as with the two-dimensional hydrogen atom, which may arise from the fact that the dSVr equations collect not only the most convex and concave neighbourhoods, but also the flattest points. For the toy model, the redundant lines can be removed by careful asymptotic analysis, leaving results that also fit intuition. As for the Lorentzian signature, however, it can happen that no result fully agrees with intuition, as we have seen in the modulated toy model. We have to decide whether to believe in mathematics and abandon our intuition, or stick to the intuition and find a better mathematical description. Finally, an algorithm is needed to find the contour ridgelines for numerically constructed wave packets. This is to be investigated in the future.

Lastly, the stream approach to ridgelines, which dates back to Rudolf Rothe in 1915, tells us to solve for a generic first integral w of the gradient vector field from Eq. (74), so that an inverse integral factor θ can be calculated, and $\theta = 0$ gives the singular stream lines, that define the stream ridgelines. As has been shown with Fig. 14(c), it can give results that are also directionally minimal. With the Euclidean signature, directions of the gradient vector field give the fastest ascent. The stream approach here gives results that agree with intuitive expectations, and no redundant lines appear except for those given by symmetries. We have shown this with the helicoidal gutter, as well as the toy model $\rho = \mathrm{e}^{-f^2}$ analytically; numerically, the modulated toy model $\rho = g\mathrm{e}^{-f^2}$ as well as the two-dimensional hydrogen atom also seems to perform pretty well under this approach. As for the Lorentzian signature, the singular stream lines of the gradient vector field do not seem to agree with the intuitive ridgelines, as we have seen in the numeric results of the "linear" wave packet in Fig. 13(b). The reason is that, for Lorentzian geometry, the directions of the gradient vector field differ from those of the gradient one-form field, and the former field no longer points to the direction of the fastest ascent. One can either discard intuition and embrace what mathematical generalization gives, or invent a novel notion of ridgelines, keeping in mind that this new notion is also to work with the Euclidean case. Finally, an algorithm is needed to find the singular ridgelines for an analytically given gradient vector field, since the generic first integral is difficult to solve. Moreover, for the cases where wave packets are already constructed numerically, another algorithm is needed to find the singular ridgelines from the numerically given gradient vector field.

The systematics of ridgelines enables us to *calculate* the classical trajectories that emerge from a quantum wave packet with *arbitrary* width. In Fig. 5, for example, one sees three trajectories, one of which coincides or is close to a classical trajectory; with the profile of the wave packet considered, one may understand it as predicting a *tunneling* between two branches of the wave packet, in that the wave packet describes a semiclassical universe evolving from one classical trajectory in the asymptotic region to *another* classical trajectory, tunneling near the origin of the plot. In contrast, the other two trajectories depart from classical trajectories near the classical turning point, giving a semiclassical behavior that essentially differs from the classical one. The tunneling picture can be useful for the singularity avoidance, which also tells a semiclassical fate.

ACKNOWLEDGMENTS

The authors would like to thank Claus Kiefer (Cologne) in particular, for critically reading the manuscript and providing valuable comments at various stages of this work. Y.-F. W. is also grateful to Nick Kwidzinski (Düsseldorf), Leonardo Chataignier (Bologna), Tim Schmitz (Leverkusen), and Ziping Rao (Melbourne). C. L. was supported by the Fundamental Research Funds for the Central Universities, Nankai University under Grant No. 63201006. Y.-F. W. was supported by the Bonn-Cologne Graduate School of Physics and Astronomy (BCGS).

APPENDIX: SEMICLASSICAL APPROACH OF WKB

The WKB approach, named after Wentzel, Kramers and Brillouin [53–55], is an important approximation in conventional quantum mechanics that separates the rapidly varying phase from the slowly varying amplitude [[56], Vh. 7; [1], Sec. 5.3.2]. It is also one of the standard ways to connect quantum geometrodynamics with classical general relativity.

In contrast, the connection between the quantum and classical gravitational theories in the scenario of *wave packets*, is not very clear, and mostly *ad hoc* case by case, shown with plots [8,9,18]. In [57], the author observed that a superposition of WKB states can be chosen to have support only in a thin "tube" around a classical trajectory. Moreover, in [58], it was suggested that in the WKB approximation an integral across a narrow section near a classical trajectory is related to the lapse function. Furthermore, in [59], the author interpreted WKB wave packets as containing higher-order WKB effects. And finally, in [60], it was suggested that the wave function of the universe forms a narrow wave packet in the classical region.

It is common to construct a wave packet by superposing mode functions with an amplitude that refers to a quantum number, e.g., superposing plane waves with a Gaussian amplitude that refers to the momenta of the plane waves. At the classical level, the quantum numbers correspond to first integrals, and using the former implies the existence of the latter. Therefore, this practice implicitly assumes that the system is *Liouville integrable* [[61], Sec. 49], containing a number of first integrals. Systems that do not have sufficient first integrals belong to the regime of classical

and quantum chaos [62], and will not be studied here. For a criterion of integrable systems that can be separated in the Hamilton–Jacobi formulation, see [63].

In this Appendix, we will first describe the general WKB theory in mathematics and minisuperspace models, and explain the relation between the WKB mode functions and the classical trajectories in Sec. A 1. Then we will derive the WKB approximation for our prototype minisuperspace model, both by analyzing the obtained exact solution in Sec. A 2, and by working the WKB mode functions out from scratch in Sec. A 3. Observing that these mode functions all contain a quantum number, we will show in Sec. A 4 that these quantum numbers have their correspondence at the classical level as first integrals of the system, and the phase of the WKB mode functions is just the Hamilton's principal function. Finally, we will apply the theory established in Sec. A 4 to wave packets in Sec. II B. We will show that these wave packets, if constructed by superposing the WKB mode functions with a narrow Gaussian amplitude, necessarily peak near a classical trajectory, which has the first integrals corresponding to the center of the Gaussian amplitude.

1. General theory

This section briefly introduces the WKB approximation in mathematics and the Wheeler–DeWitt approach.

Mathematically, the WKB approximation belongs to the class of *global* approximations to the solution of a linear differential equation, in which the highest derivative is controlled by a small parameter δ [[64], Ch. 10], with respect to which the solution $y = y(x)$ is expanded as a formal power series on the exponent

$$\phi(x) \sim \exp\left(\frac{1}{\delta}\sum_{n=0}^{+\infty}\delta^n S_n(x)\right), \qquad \delta \to 0. \tag{A1}$$

In conventional quantum mechanics as well as in the Wheeler–DeWitt approach of quantum gravitation, the highest derivatives are controlled by the reduced Planck constant $\hbar$. The meaning of a power expansion with respect to such a *dimensionful* quantity is questioned at the end of this subsection.

At the next-to-leading order, the WKB wave function is often taken as the test solution [18]

$$\psi \approx \sqrt{D}\mathrm{e}^{\frac{\mathrm{i}}{\hbar}S}, \tag{A2}$$

where S is the leading-order term, $D = \mathrm{e}^{\hbar^0 S_1}$ corresponds to the real part of the next-to-leading-order term, which is called the *Van Vleck factor*, named after its eponymous founder [65].[1] In the minisuperspace models, inserting Eq. (A2) into the Wheeler-DeWitt equation, the resulting equations read [18]

$$0 = H_\perp\left(\chi,\gamma;\frac{\partial S_0}{\partial\chi},\frac{\partial S_0}{\partial\gamma}\right) = \frac{1}{2}\mathcal{G}^{IJ}\frac{\partial S}{\partial q^I}\frac{\partial S}{\partial q^J} + \mathcal{V}(q), \tag{A3a}$$

$$\mathcal{G}^{IJ}\frac{\partial S}{\partial q^I}\frac{\partial D}{\partial q^J} = -(\Box S)D. \tag{A3b}$$

Equation (A3a) is just the *Hamilton–Jacobi equation* for our singular system. Results for the next orders can be found in e.g. [[1], Sec. 5.4.1], and are not needed here.

2. Asymptotic expansion as a WKB approximation

In our prototype model, the exact solution of the minisuperspace Wheeler–DeWitt equation (3b) is known. The WKB approach can therefore be realized in two ways. One can start with the generic WKB result, which means the Hamilton–Jacobi equation in (A3), and then solve S_0 for it. This approach will be illustrated later in Sec. A 3. Alternatively, one can also begin with the mode functions in Eq. (4) which are exact solutions, and find an approximation for the Bessel functions that have the form of Eq. (A1). We will follow this approach in this section.

Since $\nu, x \propto \hbar^{-1}$ [cf. Eq. (5)], an approximation at *small* $\hbar$ means asymptotic expansion of the Bessel functions at *large* ν *and* x. Note that

$$\left(\frac{\nu}{x}\right)^2 = \frac{\varkappa p_\gamma^2}{12\mathrm{Vol}_3^2|V|\mathrm{e}^{q\chi}} \tag{A4a}$$

$$= \mathrm{trig}\left(\sqrt{\frac{3}{2\varkappa}}g(\gamma-\gamma_0)\right)^2 \quad \text{by substituting Eq. (2).} \tag{A4b}$$

Equation (A4b) makes sense *if* we want to study the behavior of the mode functions *near* a classical trajectory.

In such a case of fixed ν/x, the asymptotic representations belong to the "Debye" type [[69], Sec. 3.14.2]. In the following we give the leading-order results. For the $(-,+)$ case with $J_\nu(x)$, the Debye expansion reads [[31], Eq. (10.19.6)]

$$J_\nu(x) = \sqrt{\frac{2}{\pi}}(x^2-\nu^2)^{-1/4} \cdot\left\{\sin\left[\sqrt{x^2-\nu^2} - \nu\arccos\frac{\nu}{x} + \frac{\pi}{4}\right] + O(x^{-1})\right\} \qquad x > \nu, \tag{A5}$$

where $x > \nu$ holds because trig = sin for $(-,+)$, and $x = \nu$ is excluded because it is not contained in the trajectories. The mode function $\mathrm{e}^{\frac{\mathrm{i}}{\hbar}p_\gamma(\gamma-\tilde{\gamma}_0)}J_\nu(x)$ contains therefore *two* WKB branches $\sim\mathrm{e}^{\frac{\mathrm{i}}{\hbar}S_\pm}$,

[1] See [[66], Ch. 7] for a viable introduction of the Van Vleck factor; for historical remarks, see [67,68].

$$\frac{S_\pm}{\hbar} \coloneqq \frac{p_\gamma}{\hbar}(\gamma-\tilde{\gamma}_0) \pm \left(\sqrt{x^2-\nu^2} - \nu \arccos\frac{\nu}{x} + \frac{\pi}{4}\right). \quad \text{(A6)}$$

Note that we have introduced an additive constant $\tilde{\gamma}_0$ to cancel the extra constant factors and match the classical constant γ_0, which is also related to Eqs. (A16a) and (A16b). By using Eq. (A16a), one gets

$$0 = \frac{1}{\hbar}\frac{\partial S_\pm}{\partial p_\gamma} = (\gamma-\gamma_0) \mp \sqrt{\frac{2\varkappa}{3}}\frac{1}{g}\arccos\sqrt{\frac{\varkappa p_\gamma^2}{12\mathrm{Vol}_3^2|V|\mathrm{e}^{g\chi}}}, \quad \text{(A7)}$$

which leads to Eq. (2) with trig = sin.

For the $(+,-)$ case with $F_{\mathrm{i}\nu}(x)$ and $G_{\mathrm{i}\nu}(x)$, the Debye expansions at leading order read [[13], Eqs. (5.15) and (5.16)]

$$F_{\mathrm{i}\nu}(x) = \sqrt{\frac{2}{\pi}}(x^2+\nu^2)^{-1/4} \cdot \left\{\sin\left[\sqrt{x^2+\nu^2} - \nu\,\mathrm{arsinh}\frac{\nu}{x} + \frac{\pi}{4}\right] + O(x^{-1})\right\}, \quad \text{(A8a)}$$

$$G_{\mathrm{i}\nu}(x) = -\sqrt{\frac{2}{\pi}}(x^2+\nu^2)^{-1/4} \cdot \left\{\cos[\sqrt{x^2+\nu^2} - \nu\,\mathrm{arsinh}\frac{\nu}{x} + \frac{\pi}{4}\right] + O(x^{-1})\right\}, \quad \text{(A8b)}$$

where $x,\nu \in \mathbb{R}^+$ are arbitrary. Both cases contain two WKB branches. Take $F_{\mathrm{i}\nu}(x)$ as an example; one has

$$\frac{S_\pm}{\hbar} = \frac{p_\gamma}{\hbar}(\gamma-\tilde{\gamma}_0) \pm \left(\sqrt{x^2+\nu^2} - \nu\,\mathrm{arsinh}\frac{\nu}{x} + \frac{\pi}{4}\right), \quad \text{(A9)}$$

$$0 = \frac{1}{\hbar}\frac{\partial S_\pm}{\partial p_\gamma} = (\gamma-\gamma_0) \mp \sqrt{\frac{2\varkappa}{3}}\frac{1}{g}\,\mathrm{arsinh}\sqrt{\frac{\varkappa p_\gamma^2}{12\mathrm{Vol}_3^2|V|\mathrm{e}^{g\chi}}}, \quad \text{(A10)}$$

which also leads to Eq. (2) with trig = sinh. The calculation for $G_{\mathrm{i}\nu}(x)$ is essentially the same, with an extra constant phase shift $\pi/2$.

Finally, for the $(+,+)$ case, the expansion at leading order reads [[69], pp. 141–142]

$$K_{\mathrm{i}\nu}(x) = \sqrt{\frac{2\pi}{\mathrm{e}^{\pi\nu}}}(\nu^2-x^2)^{-1/4} \cdot \left\{\cos\left[\sqrt{\nu^2-x^2} - \nu\,\mathrm{arcosh}\frac{\nu}{x} + \frac{\pi}{4}\right] + O(x^{-1})\right\} \quad \nu > x, \quad \text{(A11)}$$

where $\nu > x$ holds because trig = cosh for $(+,+)$. Equation (A11) contains, once again, two WKB branches, and one has

$$\frac{S_\pm}{\hbar} = \frac{p_\gamma}{\hbar}(\gamma-\tilde{\gamma}_0) \pm \left(\sqrt{\nu^2-x^2} - \nu\,\mathrm{arcosh}\frac{\nu}{x} + \frac{\pi}{4}\right), \quad \text{(A12)}$$

$$0 = \frac{1}{\hbar}\frac{\partial S_\pm}{\partial p_\gamma} = (\gamma-\gamma_0) \mp \sqrt{\frac{2\varkappa}{3}}\frac{1}{g}\,\mathrm{arcosh}\sqrt{\frac{\varkappa p_\gamma^2}{12\mathrm{Vol}_3^2|V|\mathrm{e}^{g\chi}}}, \quad \text{(A13)}$$

which, again, lead to Eq. (2) with trig = cosh.

3. WKB approximation by direct calculation

In this section, we obtain the WKB phase S and the Van Vleck factor D directly from Eqs. (A3a) and (A3b).

To begin with, one can verify that the $S_\pm$ given by Eqs. (A6), (A9), and (A12) are indeed complete integrals of the Hamilton–Jacobi equation (A3a), which is a *nonlinear* first-order partial differential equation by itself.

The transport equation (A3b) in our prototype model reads

$$\mathsf{s}\frac{\hbar}{\mathrm{Vol}_3}\left(-\frac{\varkappa}{6}\frac{\partial S}{\partial\gamma}\frac{\partial D}{\partial\gamma} + \mathsf{l}\frac{\partial S}{\partial\chi}\frac{\partial D}{\partial\chi}\right) = -\frac{\mathsf{s}}{\mathrm{Vol}_3}\left(-\frac{\varkappa}{6}\frac{\partial^2 S}{\partial\gamma^2} + \mathsf{l}\frac{\partial^2 S}{\partial\chi^2}\right)D, \quad \text{(A14)}$$

which is a first-order *linear* partial differential equation. By using the transformation in Eq. (5), we are able to derive the *general* integral, which contains an arbitrary *function* D_0, contrary to the *complete* integrals for S, where merely arbitrary *constants* are present. See Table IV.

Since $S_\pm$'s are complete integrals that result from separation test solutions [see Eq. (A18) below], the full Van Vleck factor should also be in a separated form, which would render D_0 constant, because it mixes γ with χ otherwise. This can be verified if one begins from scratch

TABLE IV. General integrals of the Van Vleck factor $D_\pm$ that are solutions to Eq. (A14) and correspond to $S_\pm$. The prefactors are in accordance with those in Eqs. (A5), (A8a), (A8b), and (A11). The arbitrary function D_0 can be argued to be a constant.

(l,sv)	$D_\pm$
$(-,-)$	No solution
$(-,+)$	$(+x^2-\nu^2)^{-1/2}D_0\left(\sqrt{\frac{3}{2\varkappa}}g\gamma \mp \arccos\frac{\nu}{x}\right)$
$(+,-)$	$(+x^2+\nu^2)^{-1/2}D_0\left(\sqrt{\frac{3}{2\varkappa}}g\gamma \mp \mathrm{arsinh}\frac{\nu}{x}\right)$
$(+,+)$	$(-x^2+\nu^2)^{-1/2}D_0\left(\sqrt{\frac{3}{2\varkappa}}g\gamma \mp \mathrm{arcosh}\frac{\nu}{x}\right)$

by inserting the WKB wave function in Eq. (A2) into the Wheeler–DeWitt equation (3b), and then adapts a separation test solution. An ordinary differential equation in χ would arise, from which one could find the second terms of $S_\pm$'s in Eqs. (A5), (A8a), (A8b), and (A11) that only contain γ, and the corresponding $D_\pm$'s are solved by the prefactors in Table IV, with no place for the arbitrary function D_0.

We conclude that Eqs. (A3b) and (A14) may not be the best starting point to solve for the Van Vleck factor for systems with multiple degrees of freedom.

4. WKB phase as a complete integral

In this Sec. A 4, we study the WKB mode functions and their phases. We will see that the mode functions can be chosen, such that they are labeled with quantum numbers, which are related to classical integrals of motion. Correspondingly, their phases are complete integrals of the classical Hamilton–Jacobi equation, which contain the classical integrals mentions above.

For the Hamilton–Jacobi equation (A3a), the useful family of solutions is the *complete solution* or *complete integral* [[70], Sec. 47; [52], Sec. 3.1; Sec. 9.4] that contain integral constants, e.g.,

$$S = S(q^i; \alpha_1, \ldots, \alpha_{n-1}) + \alpha_n, \tag{A15}$$

where α_i are constants, $i = 1, 2, \ldots, n$. A classical trajectory that corresponds to this WKB solution can then be obtained by the *principle of constructive interference* [57], as

$$\frac{\partial S}{\partial \alpha_i} = 0. \tag{A16a}$$

Meanwhile, in the classical Hamilton–Jacobi formalism, the related equations are

$$\frac{\partial S}{\partial \alpha_i} = \beta_i, \tag{A16b}$$

where $\{\alpha_i\}$'s are the constants contained in the complete integral S, and $\{\beta_i\}$'s are another set of constants [[70], Sec. 47].

Now, if S is a complete integral in the form of Eq. (A15), a stationary wave packet can be constructed by smearing out each constant with an amplitude; see e.g., Sec. II B.

In practice, it has been shown in [57] that, in order to be able to derive the Hamilton equations for the canonical momenta in full geometrodynamics, it is sufficient and necessary that S is a complete integral of the Hamilton–Jacobi equation, containing a number of constants that are equal to the physical degrees of freedom.

In the following we give a construction, in which the phase factor S in Eq. (A2) is indeed of a form close to the expression in Eq. (A15). Let the system be such that $m \leq n-1$ variables can be iteratively separated [[70], Sec. 48], so that the following equations can be obtained along a classical trajectory,

$$\phi_1\left(q^1, \frac{\mathrm{d}S_1}{\mathrm{d}q^1}\right) =: \alpha_1, \qquad \phi_2\left(q^2, \frac{\mathrm{d}S_2}{\mathrm{d}q^2}; \alpha_1\right) =: \alpha_2, \ldots,$$
$$\phi_m\left(q^m, \frac{\mathrm{d}S_n}{\mathrm{d}q^m}; \alpha_1, \ldots, \alpha_{m-1}\right) =: \alpha_m, \tag{A17}$$

and the corresponding complete integral, (A15), reads

$$\begin{aligned} &S(q^1, \ldots, q^n; \alpha_1, \ldots \alpha_m) \\ &= S_1(q^1; \alpha_1) + \cdots + S_m(q^m; \alpha_1, \ldots, \alpha_m) \\ &\quad + S_{m+1}(q^{m+1} \ldots q^n; \alpha_1, \ldots, \alpha_m). \end{aligned} \tag{A18}$$

From the Hamilton–Jacobi theory, we know that $\{\phi_j(q^j, p_j)\}$'s are *in involution* [[61], Sec. 10.1] with $H_\perp$, i.e., the Poisson brackets vanish,

$$[\phi_j(q^j, p_j), H_\perp(q^1, \ldots, q^n, p_1, \ldots, p_n)]_{\mathrm{P}} = 0, \quad \forall\, j = 1, \ldots, m. \tag{A19}$$

Furthermore, we require that $\{\phi_j(q^j, p_j)\}$'s are in *mutual* involution.

Upon canonical quantization, the $H_\perp$ and $\{\phi_j\}$'s are promoted to (if necessary, *self-adjoint*) operators [[1], Sec. 5.1], and the condition of mutual involution with respect to $[\cdot,\cdot]_{\mathrm{P}}$ is promoted to commuting $\frac{1}{\mathrm{i}\hbar}[\cdot,\cdot]_-$. Equation (A17) is promoted to the simultaneous eigenvalue equations

$$\phi_1\left(q^1, \frac{\hbar}{\mathrm{i}}\partial_1\right)\psi = \alpha_1\psi, \qquad \phi_2\left(q^2, \frac{\hbar}{\mathrm{i}}\partial_2; \alpha_1\right)\psi = \alpha_2\psi,$$
$$\ldots, \qquad \phi_n\left(q^n, \frac{\hbar}{\mathrm{i}}\partial_m; \alpha_1, \ldots, \alpha_{m-1}\right)\psi = \alpha_m\psi, \tag{A20}$$

so that one can write $\psi = \psi_{\alpha_1 \ldots \alpha_m}$. Applying a WKB test solution to Eq. (A20) results in the WKB wave function in Eq. (A2) with S given by Eq. (A18). This finishes our construction.

[1] C. Kiefer, *Quantum Gravity*, 3rd ed., International Series of Monographs on Physics (Oxford University Press, New York, 2012), 10.1093/acprof:oso/9780199585205.001.0001.

[2] M. Bojowald, Quantum cosmology: A review, Rep. Prog. Phys. **78**, 023901 (2015).

[3] M. P. Dąbrowski, C. Kiefer, and B. Sandhöfer, Quantum phantom cosmology, Phys. Rev. D **74**, 044022 (2006).

[4] A. Y. Kamenshchik, A. Tronconi, and G. Venturi, The Born–Oppenheimer approach to quantum cosmology, Classical Quantum Gravity **38**, 155011 (2021).

[5] J. J. Halliwell, Introductory lectures on quantum cosmology, in *Quantum Cosmology and Baby Universes*, Vol. 7, edited by S. Coleman, J. B. Hartle, T. Piran, and S. Weinberg (World Scientific, Singapore, 1991), 10.1142/9789814503501_0003.

[6] Y. Kazama and R. Nakayama, Wave packet in quantum cosmology, Phys. Rev. D **32**, 2500 (1985).

[7] C. Kiefer, Wave packets in minisuperspace, Phys. Rev. D **38**, 1761 (1988).

[8] C. Kiefer, Wave packets in quantum cosmology and the cosmological constant, Nucl. Phys. **B341**, 273 (1990).

[9] A. A. Andrianov, C. Lan, O. O. Novikov, and Y.-F. Wang, Integrable minisuperspace models with Liouville field: energy density self-adjointness and semiclassical wave packets, Eur. Phys. J. C **78**, 786 (2018).

[10] A. A. Andrianov, O. O. Novikov, and C. Lan, Quantum cosmology of multifield scalar matter: Some exact solutions, Theor. Math. Phys. **184**, 1224 (2015).

[11] A. A. Andrianov, C. Lan, and O. O. Novikov, PT symmetric classical and quantum cosmology, in *Springer Proceedings in Physics* (Springer, New York, 2016), pp. 29–44, 10.1007/978-3-319-31356-6_3.

[12] B. S. DeWitt, Quantum theory of gravity. I. The canonical theory, Phys. Rev. **160**, 1113 (1967).

[13] T. M. Dunster, Bessel functions of purely imaginary order, with an application to second-order linear differential equations having a large parameter, SIAM J. Math. Anal. **21**, 995 (1990).

[14] I. S. Gradshteyn and I. M. Ryzhik, *Table of Integrals, Series, and Products*, 8th ed., edited by D. Zwillinger and V. Moll (Academic Press, New York, 2014), 10.1016/c2010-0-64839-5.

[15] S. B. Yakubovich, A distribution associated with the Kontorovich–Lebedev transform, Opuscula Math. **26**, 161 (2006), https://yadda.icm.edu.pl/yadda/element/bwmeta1.element.baztech-article-AGH4-0006-0012.

[16] A. Passian, H. Simpson, S. Kouchekian, and S. Yakubovich, On the orthogonality of the MacDonald's functions, J. Math. Anal. Appl. **360**, 380 (2009).

[17] R. Szmytkowski and S. Bielski, Comment on the orthogonality of the Macdonald functions of imaginary order, J. Math. Anal. Appl. **365**, 195 (2010).

[18] C. Kiefer, N. Kwidzinski, and D. Piontek, Singularity avoidance in Bianchi I quantum cosmology, Eur. Phys. J. C **79**, 686 (2019).

[19] A. Gut, *An Intermediate Course in Probability*, 2nd ed., Springer Texts in Statistics (Springer, New York, 2009), 10.1007/978-1-4419-0162-0.

[20] W. G. Unruh, Experimental Black-Hole Evaporation?, Phys. Rev. Lett. **46**, 1351 (1981).

[21] S. Weinfurtner, E. W. Tedford, M. C. J. Penrice, W. G. Unruh, and G. A. Lawrence, Measurement of Stimulated Hawking Emission in an Analogue System, Phys. Rev. Lett. **106**, 021302 (2011).

[22] J. Steinhauer, Observation of quantum Hawking radiation and its entanglement in an analogue black hole, Nat. Phys. **12**, 959 (2016).

[23] C. Barceló, Analogue black-hole horizons, Nat. Phys. **15**, 210 (2019).

[24] I. Boettcher, P. Bienias, R. Belyansky, A. J. Kollár, and A. V. Gorshkov, Quantum simulation of hyperbolic space with circuit quantum electrodynamics: From graphs to geometry, Phys. Rev. A **102**, 032208 (2020).

[25] S. Weinfurtner, S. Liberati, and M. Visser, Analogue model for quantum gravity phenomenology, J. Phys. A **39**, 6807 (2006).

[26] C. Barceló, S. Liberati, and M. Visser, Analogue gravity, Living Rev. Relativity **8**, 12 (2005).

[27] T. F. Gallagher, *Rydberg Atoms*, Cambridge Monographs on Atomic, Molecular and Chemical Physics (Cambridge University Press, Cambridge, England, 1994), 10.1017/cbo9780511524530.

[28] J. Lim, H.-g. Lee, and J. Ahn, Review of cold Rydberg atoms and their applications, J. Korean Phys. Soc. **63**, 867 (2013).

[29] N. Sibalic, *Rydberg Physics* (IOP Publishing, Bristol, 2018), 10.1088/978-0-7503-1635-4.

[30] E. E. Kummer, De integralibus quibusdam definitis et seriebus infinitis, J. Reine Angew. Math. **1837**, 228 (1837).

[31] DLMF, NIST digital library of mathematical functions, edited by F. W. J. Olver, A. B. Olde Daalhuis, D. W. Lozier, B. I. Schneider, R. F. Boisvert, C. W. Clark, B. R. Miller, B. V. Saunders, H. S. Cohl, and M. A. McClain, http://dlmf.nist.gov/, Release 1.1.2 of 2021-06-15.

[32] N. Y. Sonine, Recherches sur les fonctions cylindriques et le développement des fonctions continues en séries, Math. Ann. **16**, 1 (1880).

[33] L. Pochhammer, Ueber die Differentialgleichung der allgemeineren hypergeometrischen Reihe mit zwei endlichen singulären Punkten, J. Reine Angew. Math. **1888**, 76 (1888).

[34] X. L. Yang, S. H. Guo, F. T. Chan, K. W. Wong, and W. Y. Ching, Analytic solution of a two-dimensional hydrogen atom. I. Nonrelativistic theory, Phys. Rev. A **43**, 1186 (1991).

[35] N. Bohr, Über die Serienspektra der Elemente, Z. Phys. **2**, 423 (1920).

[36] J. A. Nelder and R. W. M. Wedderburn, Generalized linear models, Journal of the Royal Statistical Society Series A, p (Statistics in society) **135**, 370 (1972).

[37] J. J. Koenderink and A. J. van Doorn, Local features of smooth shapes: Ridges and courses, in *Geometric Methods in Computer Vision II*, edited by B. C. Vemuri (SPIE, San Diego, 1993), 10.1117/12.146617.

[38] J. J. Koenderink and A. J. van Doorn, Two-plus-one-dimensional differential geometry, Pattern Recogn. Lett. **15**, 439 (1994).

[39] D. Eberly, *Ridges in Image and Data Analysis* (Springer, New York, 1996), 10.1007/978-94-015-8765-5.

[40] B. de Saint-Venant, Surfaces à plus grande pente constituées sur des lignes courbes, Extr. Procès-Verbaux Séances Soc. Philom., Paris 24 (1852), https://www.biodiversitylibrary.org/item/98210#page/103/mode/1up.
[41] B. Markoski, *Basic Principles of Topography*, Springer Geography (Springer, New York, 2018), 10.1007/978-3-319-72147-7.
[42] C. W. Misner, K. S. Thorne, and J. A. Wheeler, *Gravitation* (Princeton University Press, Princeton, NJ, 2017) originally published in 1973.
[43] W. L. Burke, *Applied Differential Geometry* (Cambridge University Press, Cambridge, England, 1985), 10.1017/cbo9781139171786.
[44] L. D. Landau and E. M. Lifshitz, *The Classical Theory of Fields*, 4th ed., Course of Theoretical Physics Vol. 2 (Pergamon, New York, 1975), 10.1007/978-3-319-72147-7.
[45] H. Anciaux, *Minimal Submanifolds in Pseudo-Riemannian Geometry* (World Scientific, New York, 2010), 10.1142/7542.
[46] D. N. Kupeli, Degenerate submanifolds in semi-Riemannian geometry, Geometriae Dedicata **24**, 337 (1987).
[47] R. Rothe, Zum Problem des Talwegs, Sitzungsber. Berl. Math. Ges. **14**, 51 (1915).
[48] I. A. García and M. Grau, A survey on the inverse integrating factor, Qual. Theory Dyn. Syst. **9**, 115 (2010).
[49] L. R. Berrone and H. Giacomini, Inverse Jacobi multipliers, Rend. Circ. Mat. Palermo **52**, 77 (2003).
[50] V. I. Arnold, *Ordinary Differential Equations*, Universitext (Springer, New York, 1992).
[51] C. G. J. Jacobi, Theoria novi multiplicatoris systemati aequationum differentialium vulgarium applicandi, J. Reine Angew. Math. **27**, 199 (1844).
[52] L. Evans, *Partial Differential Equations*, 2nd ed., Graduate Studies in Mathematics Vol. 19 (American Mathematical Society, Providence, 2010).
[53] G. Wentzel, Eine Verallgemeinerung der Quantenbedingungen für die Zwecke der Wellenmechanik, Z. Phys. **38**, 518 (1926).
[54] H. A. Kramers, Wellenmechanik und halbzahlige Quantisierung, Z. Phys. **39**, 828 (1926).
[55] L. Brillouin, La mécanique ondulatoire de Schrödinger; une méthode générale de resolution par approximations successives, Compt. Rend. Hebd. Seances Acad. Sci **183**, 24 (1926), https://gallica.bnf.fr/ark:/12148/bpt6k3136h/f24.
[56] L. D. Landau and E. M. Lifshitz, *Quantum Mechanics*, 3rd ed., Course of Theoretical Physics (Pergamon, New York, 1977), 10.1016/c2013-0-02793-4.
[57] U. H. Gerlach, Derivation of the ten Einstein field equations from the semiclassical approximation to quantum geometrodynamics, Phys. Rev. **177**, 1929 (1969).
[58] S. W. Hawking and D. N. Page, Operator ordering and the flatness of the universe, Nucl. Phys. **B264**, 185 (1986).
[59] G. Lifschytz, S. D. Mathur, and M. E. Ortiz, Note on the semiclassical approximation in quantum gravity, Phys. Rev. D **53**, 766 (1996).
[60] Y. Ohkuwa and T. Kitazoe, Wave packet in quantum cosmology and definition of semiclassical time, Int. J. Mod. Phys. A **12**, 859 (1997).
[61] V. I. Arnold, *Mathematical Methods of Classical Mechanics*, 2nd ed., Graduate Texts in Mathematics Vol. 60 (Springer, New York, 1989), 10.1007/978-1-4757-2063-1.
[62] S. Wimberger, *Nonlinear Dynamics and Quantum Chaos* (Springer, New York, 2014), 10.1007/978-3-319-06343-0.
[63] C. Waksjö and S. Rauch-Wojciechowski, How to find separation coordinates for the Hamilton–Jacobi equation: A criterion of separability for natural Hamiltonian systems, Math. Phys. Anal. Geom. **6**, 301 (2003).
[64] C. M. Bender and S. A. Orszag, *Advanced Mathematical Methods for Scientists and Engineers I* (Mc-Graw Hill, New York, 1978), 10.1007/978-1-4757-3069-2.
[65] J. H. Van Vleck, The correspondence principle in the statistical interpretation of quantum mechanics, Proc. Natl. Acad. Sci. U.S.A. **14**, 178 (1928).
[66] W. Pauli, *Ausgewählte Kapitel aus der Feldquantisierung*, edited by U. Hochstrasser and M. R. Schafroth (ETH Zürich, Zurich, 1951).
[67] M. Visser, Van Vleck determinants: geodesic focussing and defocussing in Lorentzian spacetimes, Phys. Rev. D **47**, 2395 (1993).
[68] N. Wheeler, Feynman quantization, https://www.reed.edu/physics/faculty/wheeler/documents/Quantum Mechanics/Class Notes/Chapter 3.pdf (2000).
[69] W. Magnus, F. Oberhettinger, and R. P. Soni, *Formulas and Theorems for the Special Functions of Mathematical Physics* (Springer, New York, 1966), 10.1007/978-3-662-11761-3.
[70] L. D. Landau and E. M. Lifshitz, *Mechanics*, 3rd ed., Course of Theoretical Physics Vol. 1 (Pergamon, New York, 1976), 10.1016/c2009-0-25569-3.